



Politechnika Wroclawska

Wydział Elektroniki Mikrosystemów i Fotoniki

2017 International Students and
Young Scientists Workshop
„Optoelectronics and Microsystems”
September 8th-10th
Szkłarska Poręba, Poland



Mikroinżynieria
Mikroelektronika
Mikrosystemy



**Proceedings of
2017 International Students and Young Scientists Workshop**

“Optoelectronics and Microsystems”

8-10 September 2017, Szklarska Poręba, Poland

Wydawnictwo GMORK
Wrocław 2018

Scientific Committee:

Sergiusz Patela, Associate Professor – chairman

Leszek Golonka, Professor

Arkadiusz Dąbrowski, PhD

Paweł Knapkiewicz, PhD

Michał Krysztof, PhD

Wojciech Kubicki, PhD

Damian Nowak, PhD

Dorota Zając, PhD

Organizing Committee:

Maciej Sasowski

Wojciech Kijaszek, MSc

Dariusz Przybylski, MSc

Editors:

Sergiusz Patela, Associate Professor

Wojciech Kijaszek, MSc

Dariusz Przybylski, MSc

Cover design:

Marta Turkiewicz

Sponsorship:

Faculty of Microsystem Electronics and Photonics, Wrocław University of Science and Technology

All rights reserved. No part of this book may be reproduced, stored in a retrieval system, or transmitted in any form by any means, without the prior permission in writing of the Publisher and the copyright owners.

© Copyright by Wydawnictwo Gmork, Wrocław 2018

Wydawnictwo Gmork Swiatkowska Ryba Sp.j.

Ignacego Domeyki 16, 53-209 Wrocław, Poland

<http://www.gmork.pl>; e-mail: wydawnictwo@gmork.pl

ISBN: 978-83-948322-5-4

TABLE OF CONTENTS

Introduction	6
Laser Interference Lithography using short coherence length picosecond pulsed laser <i>M. Ćwikła, A. Zakrzewski, J. Reiner</i>	7
In situ observation of LIPSS formation based on Fraunhofer Diffraction <i>P. Dzienny, A. J. Antończak</i>	14
Algorithm of selecting the most probable Scattering Mechanism in AlGaIn/GaN type HEMT Heterostructures <i>M. Glinkowski, B. Paszkiewicz</i>	21
Alloyed ohmic contacts compositions to AlGaIn/GaN Heterostructures without Al <i>G. Ilgiewicz, W. Macherzyński, R. Paszkiewicz</i>	26
LTCC microreactor utilizing Dielectric Barrier Discharge (DBD) <i>I. Indyka, J. Macioszczyk, L. Golonka</i>	31
Data Mining to power quality issues <i>M. Jasiński</i>	37
Influence of average molar mass of polyethylenimine on gold nanoparticles synthesis <i>E. Kuc, O. Rac-Rumijowska, M. Fiedot-Toboła, E. Sęsiadek, H. Teterycz</i>	41
Encapsulated quantum dots as biocompatible imaging agents for cancer diagnosis <i>K. C. Nawrot, M. Nyk</i>	47
Optical measurements of colloidal semiconductor quantum dots photocatalytic activity <i>W. Nawrot, M. Fiedot-Toboła, K. Malecha</i>	53
Atomic Frequency Standard <i>J. Niemczuk, P. Knapkiewicz</i>	59
Application of deep reactive ion etching for nanostructuring of GaN structures <i>S. Owczarzak, A. Stafiniak, R. Paszkiewicz</i>	66

Elaboration of AR-series resists based photolithography for microelectrical devices fabrication	71
<i>A. Piejko, J. Prazmowska, R. Paszkiewicz</i>	
3D printed membrane-based gas microflow regulator	76
<i>A. Podwin</i>	
Influence of boundary conditions on results of numerical analysis of photonic devices	80
<i>D. Przybylski, S. Patela</i>	
The flow system for the non-enzymatic determination of urea	86
<i>Sz. Sobota, K. Malecha</i>	
Author Index	92

INTRODUCTION

The 2017 International Students and Young Scientists Workshop “Optoelectronics and Microsystems” brought together students, PhD students, experienced scientists and experts interested and working in novel technologies within the field of optoelectronics, telecommunications, photonics and microsystems. This event was a perfect platform for information and experience exchange and an excellent opportunity for the first presentation for many student participants.

The Workshop, organized by the Faculty of Microsystem Electronics and Photonics of Wrocław University of Science and Technology was the 18th event in this series. The tradition of the Workshop goes back onto the collaboration in the field of photonics and scientific exchange between Technische Universität Dresden and Wrocław University of Science and Technology.

8 invited talks and 22 presentations were presented during the Workshop. The subjects of the presentations covered topics such as novel applications of microsystems, photovoltaics, sensors, telecommunication, computer simulations, thin film characterization and microelectronic technology. Among the participants of the Workshop were representatives of Industrial Companies. The industrial experts presented novel technologies introduced in telecommunication, microelectronic and digital devices or systems. The workshop brought together 50 participants.

The book contains paper submissions of contributions presented by the participants during the Workshop and reviewed by the Scientific Committee. The organizing Committee would like to take the opportunity to thank all participants for high scientific level of their presentations and contributions.

Members of the Organizing Committee

LASER INTERFERENCE LITHOGRAPHY USING SHORT COHERENCE LENGTH PICOSECOND PULSED LASER

M. Ćwikła, A. Zakrzewski, J. Reiner

Faculty of Mechanical Engineering, Wrocław University of Science and Technology,
Łukasiewicza 5, 50-371 Wrocław, Poland

Abstract *The article presents laser lithography method which is used to create periodic patterns on a surface. The method uses light wave interference phenomenon. Moreover, the presentation describes the influence of the process parameters on the quality of the fabricated pattern. The first harmonic (355 nm) of solid state Nd:YVO₄, the pulsed laser has been used to fabricate interference patterns. The utilized laser is characterized by very short coherence length (1.8 mm) and constant pulse width of 10 ps. This short coherence length induced precise alignment of the optical paths due to the necessity of keeping coherence path of the beams. This issue is a novelty in Laser Interference Lithography researches. As a result of exposing a photoresist layer, one- and two-dimensional structure has been achieved. The fabricated structure had approximately 0.9 μm pattern period. Obtained result was compatible with theoretical calculations.*

Keywords: lithography, interference, microstructuring, picosecond laser, short coherence length

1. INTRODUCTION

Utilization of lithography methods can be commonly found in microelectronics, during the process of production of elements and formation of conductive paths. Depending on the way of mapping desired shape and geometry few different lithography methods can be distinguished. The most widely used method is photolithography, which is based on transferring image from a photomask to a photoresist layer through exposure with UV light [1].

Laser Interference Lithography (LIL) does not require photomask and allows to fabricate high-resolution one-, two- or three-dimensional periodical structures over a large area. LIL method is based on the phenomenon of interference between two or more laser beams. In the spot of coinciding of the waves, change of amplitude occurs [2]. There are two types of interference – constructive, which is an amplification of the variation, and destructive, which is the extinction of the variation. To create periodically patterned structure, light waves need to be coherent and monochromatic [3]. These conditions are met by laser radiation.

In order to expose surface, both pulsed (PW) and continuous wave (CW) operation lasers can be used. The Periodic pattern can be recorded on the photoresist layer, and afterward transferred to target surface through the process of dry or wet etching, furthermore PW lasers are characterized by higher power density, and they can be used to record interference patterns directly on the material surface through ablation phenomenon.

The critical factor while designing process of LIL is coherence length of the utilized laser. Interference phenomenon can only occur while the difference between separated optical

paths is less than coherence length value. In case of CW lasers, coherence length can exceed dozens of meters, whereas coherence length of PW lasers is around few millimeters [4]. Thus, utilization of pulsed lasers is associated with the necessity of precise adjustment of the optical system. That is the reason why the number of research about LIL method using pulsed lasers is smaller than in case of continuous-wave operation lasers.

The paper includes the results of photoresist exposition based on dual beam laser interference lithography. The one and two-dimensional microstructures with 0.9 μm pattern period were fabricated using picosecond laser characterized by very short coherence length (1.8 mm). Moreover, the experimental results were confirmed by theoretical investigations.

2. MATERIALS AND METHODS

2.1 Numerical analysis

The laser interference lithography technique is based on splitting a coherent laser beam and then overlapping separated beams on the target surface of the material. Consequently, the interference pattern is recorded. The basic parameter defining the resulting pattern is the disturbance period Λ , whose value depends on the light source wavelength λ and the angle between the interfering beams θ [5]:

$$\Lambda = \frac{\lambda}{2 \cdot \sin\left(\frac{\theta}{2}\right)} \quad (1)$$

The Matlab script has been mapped out to theoretically determine the period Λ (Fig. 1) Values of the parameters posited in the conducted analysis are equal to values in the performed experiment. Wavelength was $\lambda=355$ nm, the angle between interfering beams was approximately $\theta=23^\circ$. The value of the obtained period was 0.9 μm .

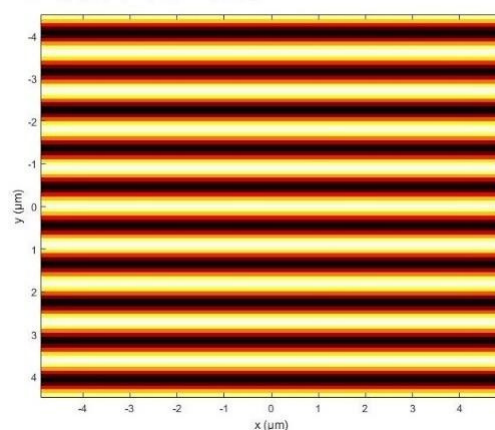


Fig. 1. Theoretical simulation of the periodic pattern for two interfering beams.
Wavelength $\lambda = 355$ nm, the angle between interfering beams $\theta = 22.62^\circ$

2.2 Optical system design

Based on the results of the Matlab simulation, the dual beam optical system for LIL was set (Fig. 2) [5]. Taking into account the value of pulse width and generated wavelength, a coherence length of 1.8 mm was determined. The generator beam *1* was routed through the reflecting mirror *2* to the 50:50 beam splitter *3*. UV prisms *4* mounted on ThorLabs XYT1/M moveable stage with a resolution of 10 μm were used to align the optical paths. This method allowed to maintain the difference of optical paths length of beams within the tolerance range defined by the coherence length. It was a critical condition to obtain an interference pattern on the sample surface. Divided beams were reflected and routed to the surface of the sample. The angle between interfering beams was approximately 23° .

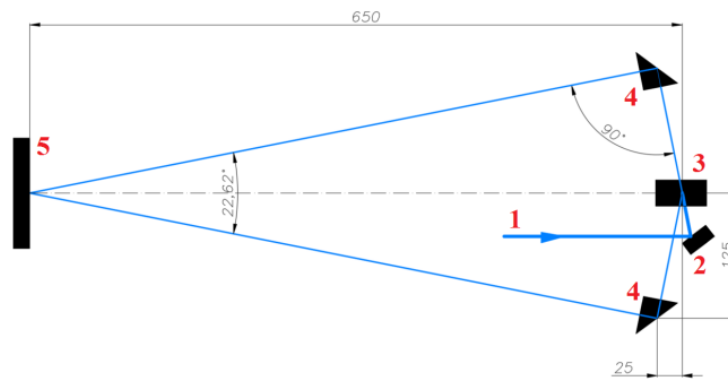


Fig. 2. Scheme of the compiled interference lithography optical system. 1 – laser beam from generator 2 – reflecting mirror, 3 – beam splitter, 4 – prism, 5 – movable stage with the mounted sample

2.3 Preparation of the surface

Duetto laser used in the following research is characterized by 1.6 MW/cm^2 of maximum power density and 1.5 mm of laser spot diameter [4]. Thus, it is possible to achieve structuring through ablation. However, in this paper, results of exposing photoresist layer has been presented due to the main purpose to prove the possibility of adjustment an optical system for LIL, using laser characterized by the very short coherence length of 1.8 mm. Exposed material was negative photoresist ma-N 1400 supplied by Micro Resist Technology company. Cleaned glass coverslips (10 x 10 mm) has been used as a base for the photoresist. The spectral sensitivity of used photoresist was in the range of 310 to 400 nm. The photoresist layer was evenly covered over glass substrate due to the process of spin coating. The rotation speed of the process was 3000 rpm [6]. Time of the process was 30 seconds and it was defined as a result of the idea of achieving the possibly thinnest layer. Above this time threshold, thickness depletion was not observed. Measured photoresist layer thickness was approximately 2 μm .

Measurement of photoresist thickness was made on LEXT OLS4000 confocal microscope (Fig. 3). The black color was profile shape of the layer, whereas the spacing between parallel green lines was measured thickness. A noticeable increase in layer thickness (black curve) was observed on the edges of the photoresist layer. The phenomenon is called Edge Bead and it was confirmed by existing research [7].

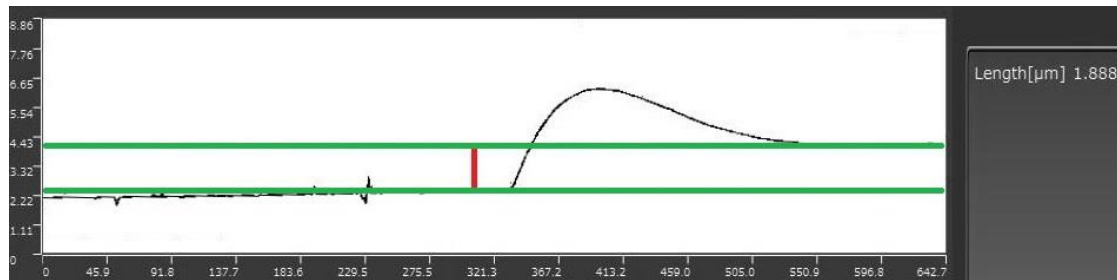


Fig. 3. Measurement of photoresist thickness, made using LEXT OLS4000 confocal microscope

The thickness of the layer was measured in few spots and it was alleged to be consistent. Lastly, the sample was subjected to a soft baking process. The process is based on the heating sample in order to remove remaining solvent concentration and improving physicochemical properties, such as increasing adhesion and reducing viscosity. Hotplate was used to heat up the sample. According to research, the temperature of heating should be 100°C and the time of the process should be 1 minute for each micrometer of the layer thickness. Too short baking or too low temperature of the process can result in foaming nitrogen bladders during exposure and increasing amount of time needed for further development (dark erosion). Too long baking causes decay of photoactive compound of the photoresist, thus lowering quality of fabricated pattern [8-9].

Due to the measured thickness of approximately of 2 μm, samples were soft baked at the temperature of 100°C and time of 2 minutes.

After spin coating and soft baking samples were exposed to UV laser beam and then developed in the ma-D 533/S developer, supplied by Micro Resist Technology. The development time has been analyzed depending on the degree of removal of unexposed photoresist areas. It has been defined that the amount of time needed to completely remove unexposed areas is 20 seconds.

3. EXPERIMENT

Duetto Time-Bandwidth Nd:YVO4 pulsed laser with a pulse width of 9.7 ps and pulse repetition frequencies range from 5 Hz to 8.2 MHz was used. The minimum energy density needed to expose negative photoresist ma-N 1400 was 300 mJ/cm² and the maximum was 700 mJ/cm² [6]. The diameter of the laser beam spot was 1.5 mm. Based on these data theoretical energy density G , provided by single pulse was calculated. Energy density was given by $G = E/A$, where A is a cross section area of the laser spot and it was defined by $\pi d^2/4$. Calculations were made with the assumption of a maximum total power of 3 W and single pulse energy of 60 μJ. The energy density in single pulse was 3.4 mJ/cm². Thus, the minimum number of pulses needed to record pattern on the photoresist was approximately 89. The minimum number of pulses is desirable from the viewpoint of the quality of the resulting interference pattern. As more pulses are dispensed to the substrate, the greater the degeneration of the pattern. On the other hand reducing the number of pulses resulted in the underexposure of the photosensitive emulsion. The pulse repetition rate (PRF) has been set at 10 Hz. The result of exposing by 89 pulses the photoresist layer on the glass substrate was recorded by the Olympus LEXT OLS4000 confocal microscope (Fig. 4).



Fig. 4. The result of the single photoresist exposure. 89 pulses, Pulse Repetition Rate PRF = 10 Hz

Moreover, the effect of a two-dimensional interference pattern was obtained by rotating the sample around its axis by 90° and re-exposing the sample (Fig. 5). The photoresist exposure parameters were the same as for one-dimensional structures.



Fig. 5. The result of double exposure of the sample with a rotation of the substrate by 90° . 89 pulses, Pulse Repetition Rate PRF = 10 Hz

To verify the value of the period, the method of laser profile measurement by the LEXT OLS4000 microscope was done (Fig. 6). The width (the red line between two green, parallel lines) is the measured period Λ .



Fig. 6. Profile measurement of the distance between interference fringes

The determined value Λ is in agreement with the values obtained during the numerical analysis, with the accuracy of 0.1 μm . The discrepancy is due to the possible geometrical differences between designed and the actual optical system. Consequently, the difference in angle between interfering beams.

4. CONCLUSION

The possibility of fabricating periodically patterned structures by interference lithography using Nd:YVO₄ pulsed laser characterized by a very short coherence length (1.8 mm) is presented. Coupling two laser beams from the same source resulted in recording interference pattern on the surface of the photoresist. Due to the very short coherence length, an optical system was set with high accuracy using XY stages, characterized by resolution of 10 μm . As a result of exposure of the substrate, a single dimensional structure with the period of approximately 0.9 μm and total exposed area of 1.75 mm² was obtained. Moreover, a two-dimensional structure was obtained after rotating the sample by 90° and re-exposing undeveloped photoresist layer. The advantage of the LIL process over other lithography techniques is the relatively low costs, the short fabrication time, and the high resolution of recorded patterns. The method proves to be unrivaled in the case of producing thick periodic patterns on a micro scale over a large area. The utilization of high power, pulsed laser for the LIL creates the potential for surface structuring using laser ablation. This means reducing the many time-consuming manufacturing steps typical of photolithography to one - exposure. It is possible to directly fabricate the large area of materials such as metals, polymers or ceramics [2, 10].

References

- [1] M. J. Madou, *Fundamentals of Microfabrication, The Science of Miniaturization*, Second Edition, 1-71, (2002).
- [2] JH. Seo, JH. Park, Z. Ma, J. Choi, BK. Ju, *Nanopatterning by Laser Interference Lithography: Applications to Optical Devices*, Journal of Nanoscience and Nanotechnology, Volume 14, Number 2, (2014).
- [3] H. Kang, G. Hernandez, J. Zhang, Y Zhu, *Phase controlled light switching at low power levels*, American Physical Society, (2005).
- [4] *User Manual of Duetto Time-Bandwidth laser*.
- [5] H. van Wolferen, L. Abelmann, *Lithography: Principles, Processes and Materials: Laser Interference Lithography*, Nova Science Publishers, Netherlands, (2011).
- [6] *Negative Photoresists for UV & Electron Beam Lithography Flyer*, <http://www.microresist.de>, (access_08.2017).
- [7] Dr. R. B. Darling, *Photolithography*, <https://www.researchgate.net>, (access 08.2017).
- [8] *Softbake of Photoresist Films*, www.microchemicals.com/downloads/application_notes.html, (access 08.2017).
- [9] *Exposure of Photoresists*, www.microchemicals.com/downloads/application_notes.html, (access 08.2017).

- [10] A. Lasagni, C. Holzapfel, F. Mucklich, *Periodic pattern formation of intermetallic phases with long range order by laser interference metallurgy*, *Advanced Engineering Materials*, Volume 6, Number 7, (2005).

IN SITU OBSERVATION OF LIPSS FORMATION BASED ON FRAUNHOFER DIFFRACTION

P. Dzienny*, A. J. Antończak

Faculty of Electronics, Wrocław University of Science and Technology,
Wybrzeże Wyspiańskiego 27, 50-370 Wrocław, Poland
*e-mail: paulina.dzienny@pwr.edu.pl

Abstract *Laser-induced periodic surface structures (LIPSS) are highly periodic wavy surface features which are frequently smaller than the incident light wavelength, which brings possibility of nanostructuring of many materials. Although it is widely known that they can be obtained on any material, including metals, semiconductors and dielectrics, phenomena of their formation is not yet fully explained. Because of their dimensions, observation of them usually requires techniques such as SEM and AFM. A new method of observing formation in situ, based on Fraunhofer diffraction on gratings is proposed. It was developed for observing LIPSS creation under excimer laser irradiation on transparent polymers, but has a potential to be applied to different laser systems and materials.*

Keywords: LIPSS, nanostructuring, optoelectronics, polarization

1. INTRODUCTION

Laser-induced periodic surface structures (LIPSS) are regular wavy structures, in literature referred to as ripples [1], periodic patterns and self-organizing nanostructures [2]. Their amplitude and periodicity are usually in nanometer range what allows to obtain structures much smaller than it is possible with traditional methods, where the dimension of the structures is limited by the laser spot size. A necessary condition to be fulfilled to produce this structures is having polarized radiation. Although it is known that they can be obtained on virtually any material, including metals [3] [4], semiconductors [5-7], dielectrics [8-10], polymers [11, 12] and carbon-based materials [13-15], phenomena of their formation are still under debate. Works on their application are in progress. They can be diverse: biomedical (cell culture [16], culturing human embryonic kidney cells and skeletal myoblasts [17], super-hydrophobic properties [18]), decorative [19] [20], photovoltaic (LSFL on 400 nm Mo film for light trapping scattering on PV) [21], mechanical [22], as diffraction gratings for a display [20] or in microelectromechanical systems and patterning for field-emitting displays [8].

Several types of LIPSS are distinguished in the literature. The two main are low spatial frequency (LSFL) and high spatial frequency (HSFL). The first type has spatial periodicity Λ close to the laser wavelength λ and orientation orthogonal to the polarization of incident light. They form both under continuous [23] and pulsed [5] laser radiation of energy density close to ablation threshold and their amplitudes are in order of 100 nm to a few hundred. The second type has periodicity a few times smaller than the laser wavelength and can be either parallel and orthogonal to the polarization of the light. They can be obtained using only laser pulses with ultra-short duration (pico- or femtosecond regime).

Due to LIPSS usual size, their observation is possible only by using strong optical microscopes (only in case of LSF LIPSS), AFM and SEM. In this article a new method of

observing formation in situ is proposed, that does not require such advanced techniques. It is based on Fraunhofer diffraction on gratings.

2. EXPERIMENTAL

During the experiment, two materials were modified: polystyrene (PS) and poly(methyl methacrylate) (PMMA). The laser irradiation was performed using ArF excimer laser that operates at 193 nm wavelength with 6 ns pulse duration (ATLEX300-I ATL Lasertechnik GmbH). The laser output was linearly polarized with an air-spaced version of UV MgF₂ Rochon Polarizer (Bernhard Halle Nachfl. GmbH). The angular separation of the ordinary and extraordinary beam is around 0.55°. The material was placed in such distance from polarizer that beams were spatially separated on its surface. The samples were prepared with varying amount of pulses deposited on the surface, from 100 to 11 000 in order to observe its influence on LIPSS formation. The size of the beam was around 4x4 mm for each polarization.

The setup for observation of LIPSS formation employed single He-Ne laser generating 632.8 nm wavelength (figure 1). The laser beam was set to traverse the material in the precise area where LIPSS were forming, it is the area with the highest energy density distribution in excimer laser beam cross section. Created this way image was placed on the screen perpendicular to the red beam.

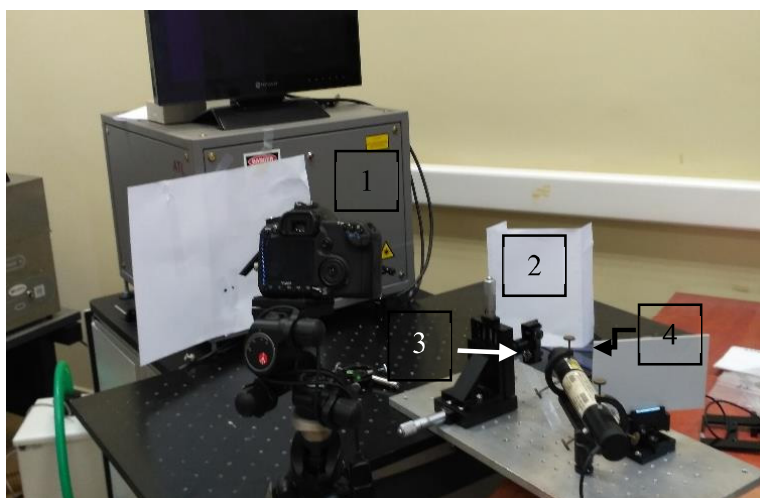


Fig. 1. Photograph of experimental setup: 1 – excimer laser; 2 – screen; 3 – sample; 4 – He-Ne laser

Microscopic images were obtained with digital microscope Keyence VHX-5000 with magnification up to 1000x. Fast Fourier Transform was prepared using ImageJ software.

3. THEORY AND RESULTS

A grating with periodicity S diffracts a normally incident beam of light of wavelength λ into a set of beams, at angles θ_n that can be described by the following equation:

$$\sin\theta_n = n\lambda/S \quad (1)$$

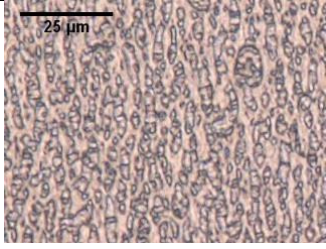

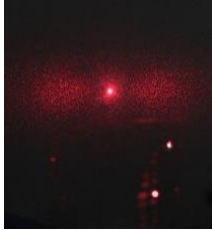
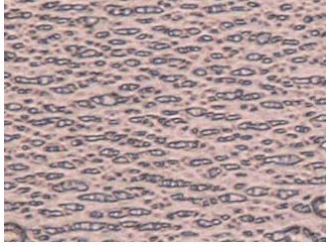
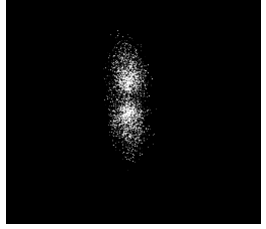
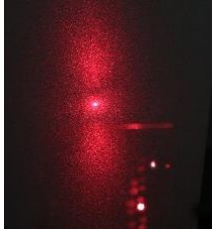
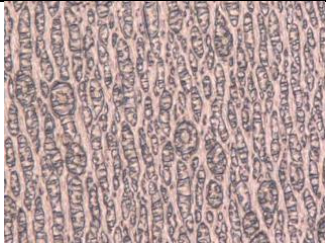
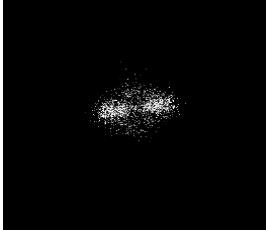

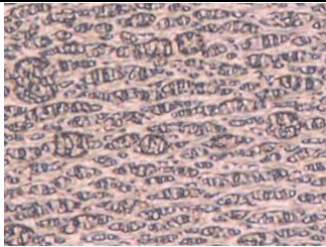
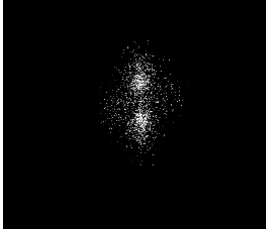
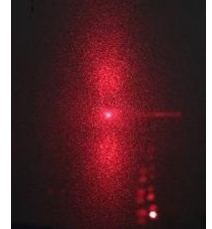
where $n = 0, \pm 1, \pm 2 \dots$

In the case when the light is incident at an angle θ_0 , the equation slightly changes:

$$\sin\theta_n = n\lambda/S + \sin\theta_0 \quad (2)$$

Above equation (2) was used to determine the periodicity of LIPSS formed on PMMA and PS (table 1 and 2).

Table 1. Microscopic images, FFT od them and Fraunhofer diffraction patterns obtained for PMMA samples; a, b – beams of different polarization

Amount of impulses and laser energy	Microscopic image	FFT of microscopic image	Photograph of Fraunhofer diffraction pattern
5.5 mJ 7500 imp a			
5.5 mJ 7500 imp b			
5.5 mJ 10 000 imp a			
5.5 mJ 10 000 imp b			



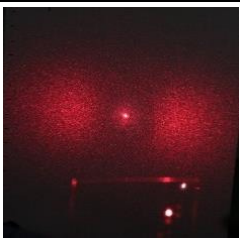
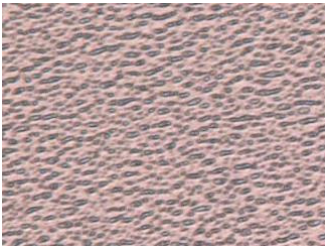
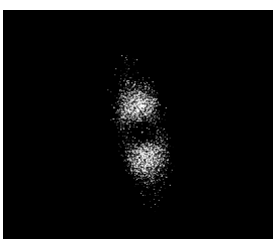
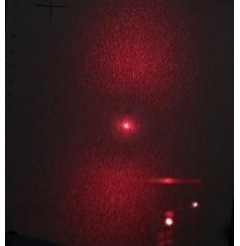
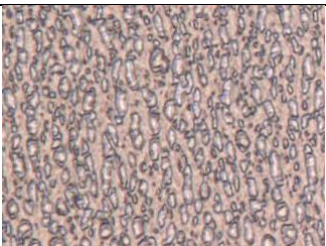
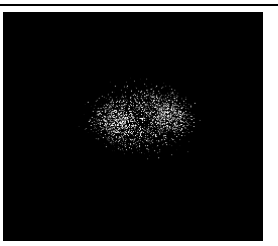
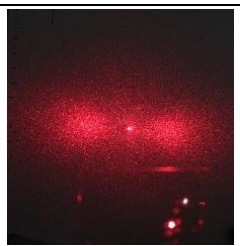
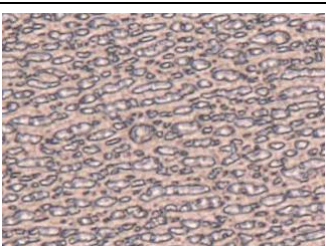
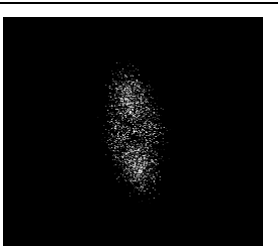
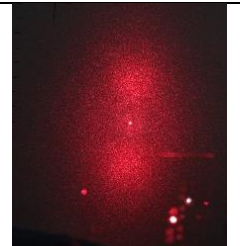
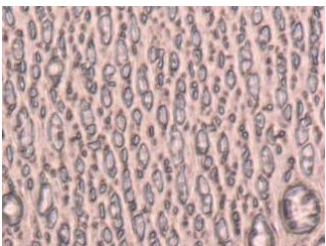
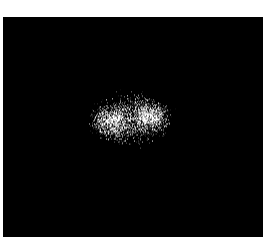
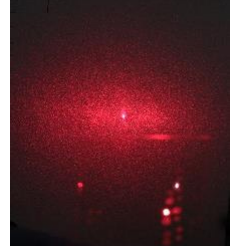
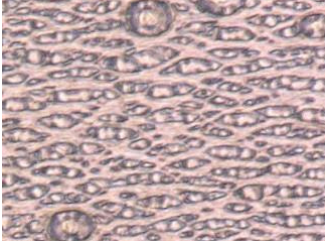
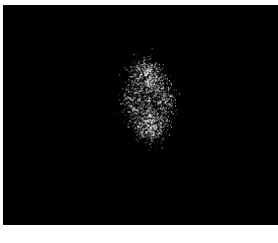
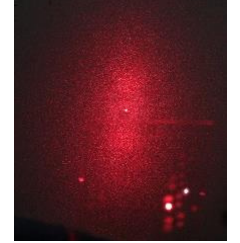
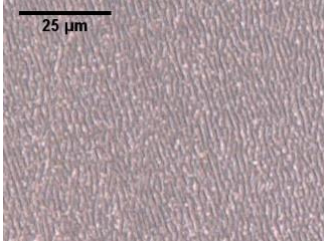
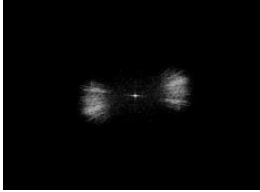





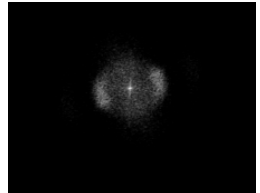

7.5 mJ 2500 imp a			
7.5 mJ 2500 imp b			
7.5 mJ 5000 imp a			
7.5 mJ 5000 imp b			
7.5 mJ 7500 imp a			
7.5 mJ 7500 imp b			

Table 2. Microscopic images, FFT of them and Fraunhofer diffraction patterns obtained for PS samples irradiated with laser energy 7.3 mJ, polarizer's ordinary beam (a)

Amount of impulses	Microscopic image	FFT of microscopic image	Fraunhofer diffraction pattern
500			
1000			
2000			

As it is visible on images gathered in table 1 and 2, the formation of LIPSS can be observed through Fraunhofer diffraction pattern changes during the process of irradiation. With increasing amount of impulses leading to gratings organization, the maximums are becoming more visible on the screen. When a certain amount of impulses is exceeded, i. e. when deposited energy is high enough to destroy the LIPSS, maxima blur. It is noteworthy that obtained LIPSS are of very poor periodicity, and the radiation traverses through the material, what is the reason why maxima are an overall blur.

For PMMA periodicity obtained from FFT of microscopic image is 3.4-5 μm , and from the Fraunhofer diffraction pattern 4-5.5 μm in dependence on laser irradiation density. In case of PS the values were 1.75 μm and 1.85 μm accordingly. The difference between values obtained using both methods (0.4 μm maximally) is small taking into consideration, that only approximate value is read due to maxima blur.

In dependence of polarization of the incident light LIPSS of orthogonal orientation were observed.

4. CONCLUSIONS

A new method allowing observing LIPSS formation in situ, based on Fraunhofer diffraction on gratings is proposed. It was developed for experiments under excimer laser irradiation on transparent polymers, but has a potential to be applied for different laser systems and materials, including non-transparent materials, as the dependence is preserved when the beam is reflected from the grating.

References

- [1] Fauchet M. P., et al. *Surface ripples on silicon and gallium arsenide under picosecond laser illumination*, Applied Physics Letters 40.9. 1982, 824-826.
- [2] Römer E., et al. *On the formation of laser induced self-organizing nanostructures*, CIRP Annals-Manufacturing Technology 58.1. 2009, 201-204.
- [3] Yong J., et al., *Laser-induced damage on single-crystal metal surfaces*, JOSA B 5.3. 1988, 648-659.
- [4] Bonse J., et al., *Sub-100-nm laser-induced periodic surface structures upon irradiation of titanium by Ti: sapphire femtosecond laser pulses in air*, Applied Physics A 110.3. 2013, 547-551.
- [5] Emmony D. C., et al., *Laser mirror damage in germanium at 10.6 um*, Applied Physics Letters 1973, 598-600.
- [6] Young F. J., et al., *Laser-induced periodic surface structure. II. Experiments on Ge, Si, Al, and brass*, Physical Review B 27.2. 1983, 1155.
- [7] Bonse J., et al., *On the role of surface plasmon polaritons in the formation of laser-induced periodic surface structures upon irradiation of silicon by femtosecond-laser pulses*, Journal of Applied Physics 106.10. 2009, 104910.
- [8] Wu Q., et al., *Femtosecond laser-induced periodic surface structure on diamond film*, Applied Physics Letters 82.11. 2003, 1703-1705.
- [9] Temple P., et al., *Polarization charge model for laser-induced ripple patterns in dielectric materials*, IEEE journal of Quantum Electronics 17.10. 1981, 2067-2072.
- [10] Dufft D., et al., *Femtosecond laser-induced periodic surface structures revisited: a comparative study on ZnO*, Journal of Applied Physics 105.3. 2009, 034908.
- [11] Baudach S., et al., *Ablation experiments on polyimide with femtosecond laser pulses*, Applied Physics A 69.1. 1999, S395-S398.
- [12] Csete M., et al., *The role of original surface roughness in laser-induced periodic surface structure formation process on poly-carbonate films*, Thin Solid Films 453. 2004, 114-120.
- [13] Zhang W., et al., *Formation of Laser-induced Periodic Surface Structures During Femtosecond Laser Ablation of Highly Oriented Pyrolytic Graphite (HOPG)*, Lasers in Engineering (Old City Publishing) 25. 2013.
- [14] Feng P., et al., *Effect of ambient air on femtosecond laser ablation of highly oriented pyrolytic graphite*, Optics letters 40.1. 2015, 17-20.
- [15] Huang M., et al., *Mechanisms of ultrafast laser-induced deep-subwavelength gratings on graphite and diamond*, Physical Review B 79.12. 2009, 125436.
- [16] Rebollar E., et al., *Physicochemical modifications accompanying UV laser induced surface structures on poly (ethylene terephthalate) and their effect on adhesion of mesenchymal cells*, Physical Chemistry Chemical Physics 16.33. 2014, 17551-17559.

- [17] Rebollar E., et al., *Proliferation of aligned mammalian cells on laser-nanostructured polystyrene*, Biomaterials 29.12. 2008, 1796-1806.
- [18] Groenendijk M., et al., *Surface microstructures obtained by femtosecond laser pulses*, CIRP Annals-Manufacturing Technology 55.1. 2006, 183-186.
- [19] Dusser B., et al., *Controlled nanostructures formation by ultra fast laser pulses for color marking*, Optics express 18.3. 2010, 2913-2924.
- [20] Yao J., et al., *Selective appearance of several laser-induced periodic surface structure patterns on a metal surface using structural colors produced by femtosecond laser pulses*, Applied Surface Science 258.19. 2012, 7625-7632.
- [21] Scorticati D., et al. *Thin film surface processing by ultrashort laser pulses (USLP)*, SPIE Photonics Europe. International Society for Optics and Photonics 2012.
- [22] Eichstädt J., et al. *Towards friction control using laser-induced periodic surface structures*, Physics Procedia 12. 2011, 7-15.
- [23] Kaneko S., et al., *Nano-strip grating lines self-organized by a high speed scanning CW laser*, Nanotechnology 22.17. 2011, 175307.

ALGORITHM OF SELECTING THE MOST PROBABLE SCATTERING MECHANISM IN ALGaN/GaN TYPE HEMT HETEROSTRUCTURES

M. Glinkowski*, B. Paszkiewicz

Faculty of Microsystem Electronics and Photonics, Wrocław University of Science and Technology,
Janiszewskiego 11/17, 50-372 Wrocław, Poland

*e-mail: mateusz.glinkowski@pwr.edu.pl

Abstract In AlGa_N/Ga_N type HEMT (High Electron Mobility Transistors) heterostructures movement of electrons is quantized in growth direction in the triangular potential well that is formed due to the big difference of AlGa_N and Ga_N band gaps. As a result the piezoelectric polarizations 2DEG (two-dimensional electron gas) is created at AlGa_N/Ga_N interface. The mobility of 2DEG can be influenced by many factors such as acoustic and optical phonons, ionized Ga_N and AlGa_N impurities, dislocations and others. To determine how electron scattering mechanism affect mobility 2DEG in AlGa_N/Ga_N type HEMT heterostructures, the algorithm of selecting the most probable 2DEG scattering mechanism based at Matthiessen rule was developed. Next applied for analysis of the Hall mobility values of AlGa_N/Ga_N HEMT type heterostructures measured at wide range of temperatures from 77K to 420K.

Keywords: heterostructure AlGa_N/Ga_N, Matthiessen rule, Python, algorithm

1. INTRODUCTION

AlGa_N/Ga_N type HEMT heterostructures due to formation of 2DEG provide a high mobility values of electrons. Mobility's describe how quickly electron can move through a metal or semiconductor when an electric field is applied. It's a qualitatively parameter of AlGa_N/Ga_N type HEMT heterostructures and also gives information how fast electronic devices could work. The truth nature of 2DEG appear under concentration of electrons less then $4.5 \times 10^{12} \text{ cm}^{-2}$. Above this concentration many subbands will be very quickly occupied and electrons will lose a true 2DEG nature. The mobility of 2DEG electrons with concentration above this value also will be lower due to the intersubband scattering [1]. For this reason also during growth process of AlGa_N/Ga_N HEMT heterostructures it's important to appropriately combine the spacer width and donor concentrations of the epitaxial structure. To calculate a theoretical 2DEG mobility in AlGa_N/Ga_N type HEMT heterostructures the Matthiessen rule was involve. Next numerical procedure using i.e. basic functions of Python 3.5 could be elaborated and as a result the developed algorithm will suggest what scattering mechanism have influence on the 2DEG mobility of studied structures.

2. MATTHIESSEN RULE

Electrons in crystal lattice usually are considered with an stationary Bloch function to describe their motion. But it well-known that this description are invalid for real materials. It's similar to describe motion of an object without considering forces of resistance or friction. In real crystals lattice electrons can't move freely because they constantly collide

with some kind of imperfections e.g. acoustic phonons, impurities, dislocations [2]. When electron collide with imperfection it will get a new value of wave vector and energy. After collision it will move freely for short period of time until next collision appears. We can notice that when we sum many of this periods we will get an average time of scattering rate. This scattering rate are different for each kind of imperfections and it's order of magnitude is in picoseconds. Electron mobility could be evaluate from following equation (1):

$$\mu = \frac{e\langle\tau\rangle}{m^*} \quad (1)$$

where: e is the charge of electron, $\langle\tau\rangle$ is the scattering rate and m^* effective mass of 2DEG. To calculate the mobility's of 2DEG for each kind of scattering mechanism it is essential to calculate first the average scattering rate for each kind of scattering mechanism. The main principle of Matthiessen rule relay on sum all reverse mobility's of each kind of scattering mechanism μ_i (2):

$$\frac{1}{\mu_{total}} = \sum_{i=1}^n \frac{1}{\mu_i} \quad (2)$$

where: μ_{total} is the total mobility of the electrons in the sample.

The main idea of simulations relay on connection between calculations of i-th theoretical mobility's combination with experimental results. The appropriate combination result in the same values. Problems can appear when important scattering mechanism which have real impact at mobility's in examined heterostructure wasn't include into theoretical calculations. This lead to higher mismatch between theoretical calculations with experimental results.

3. NUMERICAL CONCEPT OF ALGORITHM

The main idea of algorithm was to obtain a 2DEG mobility's of AlGaIn/GaN type HEMT heterostructures closest to the experimental values (that were obtained earlier from Hall measurement performed using van der Pauw structures) not by fitting the curve but by using the Matthiessen rule. So far in performed calculations only 7 scattering mechanism from about 15 was included and these results could be inaccurate but the method of the total mobility's calculation will be the same.

The performed measurements allowed to obtain the mobility of 2DEG electrons. The measurement was performed in the ranges of temperatures from 77 K to 420 K and 14 measurement points were obtained for each heterostructure. When we compare these result with theoretical scattering rates it gives 127 possibilities of combinations 7 scattering mechanism. Because it was 14 measurement points, 1778 values of mobility's was to examine.

3.1 List, Arrays and Tuples

In Python 3.5 the basic structures of data in this program are: list, array and the tuple. Each of these have unique properties. The main difference is in the mathematician operation. Concatenating two list result in a new list with length of sum of two previous and without

modifying its arguments. Concatenating two arrays result in sum of each elements in arrays and new array will have the same length as previous two. The tuple is a special case of a list. It is very similar but the value of tuple can't be changed. The last type it's very useful for dictionaries not for mathematical calculation.

3.2 Read file

To load data from text file from Hall experiment *r* (*read*) statement was used. Commands like *replace* (change unreadable symbols to whitespaces) was, *split* (distinguish each column of data) was useful. Because the text is string type *float* command was essential. All data was assigned by *append* command to appropriate variables.

3.3 Combination

To combine all scattering mechanism without repetitions module *combination* from library *itertools* was involve and appropriate statement was used.

3.4 Algorithm

In double *loop* list result from division operation of *i-th* value of sample 2DEG mobility's with *i-th* value of 2DEG mobility's of electrons from *j-th* scattering combination was added to empty list. After the division operation an initial information about connection theoretical result with experimental results was known. Using *if* statement compared the result of division with number one by using operation of addition and subtracting of small number. The number of iterations state distance between theoretical and experimental results and it gives the qualitative information potential scattering mechanism.

3.5 Data researching

After calculations numbers of iterations and assign them to appropriate variables next step is to find the lowest values for each temperature measurements points. To make this it's convenient to write your data to excel in some special way. The columns will be represent a vectors with iterations from algorithm for each kind of scattering mechanism and the rows will be the temperature. To find the closest value to the experimental we need just to find minimum value of row using *min* command.

3.6 Results

Using library *matplotlib* and module *pyplot* experimental data and theoretical result of exemplary AlGaIn/GaN HEMT heterostructure 2DEG mobility in function of temperature was shown. The results are presented in Fig. 1. In some cases of temperatures 100% agreement between measured and calculated data was obtain. It is clear that in temperature 320K electrons collides only with acoustic phonons in piezoelectric and deformation modes.

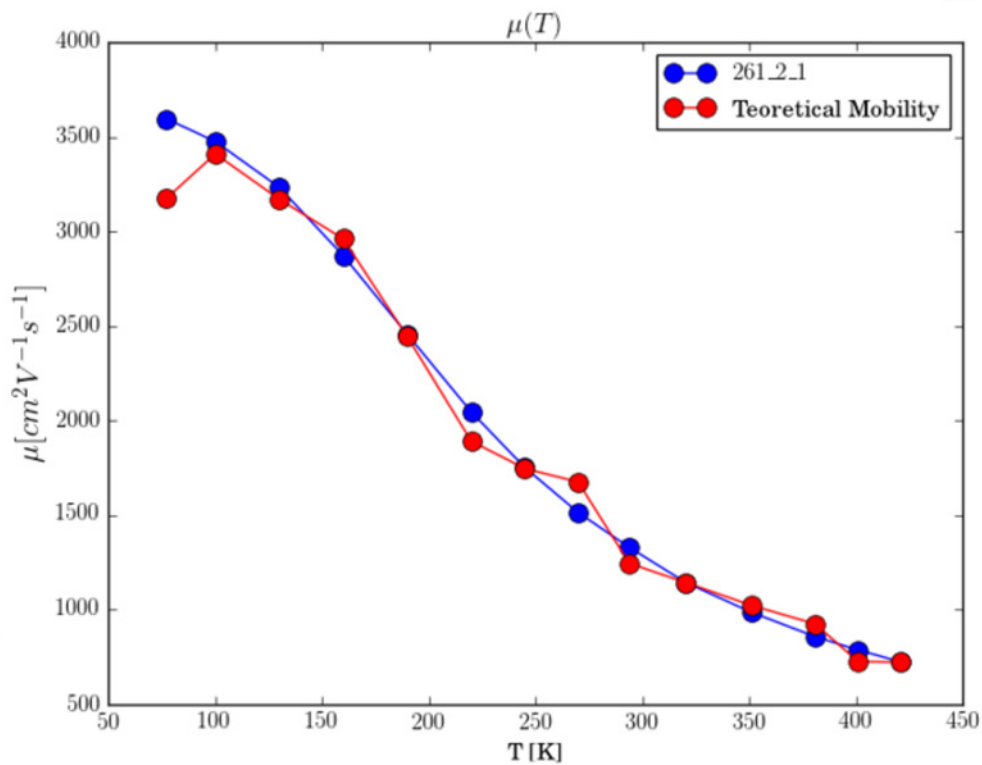


Fig. 1. Experimental data and theoretical result for mobility's of 2DEG in function of temperature are show as blue and red curve respectively

4. CONCLUSION

Calculated seven scattering mechanism in AlGaIn/GaN type HEMT heterostructures. According to the Matthiessen rule results was fit to the experimental data. Found good agreement with these data but still it is important to include other scattering mechanism to think about obtaining useful information. That information could be used for improving the technological process of heterostructures fabrication to achieve the maximum values of 2DEG mobility. It's good to make a windows application that will be more friendly for use. Calculating all existing scattering mechanism led to significant information for better understanding of the operation of devices fabricated in AlGaIn/GaN HEMT type heterostructures.

Acknowledgement

This work was co-financed by the European Union within the European Regional Development Fund, through a grant from the Innovative Economy (POIG.01.01.02-00-008/08-05), by the National Centre for Research and Development through the Applied Research Program Grant No. 178782, the program LIDER No. 027/533/L-5/13/NCBR/2014, the National Science Centre under Grant No. DEC-

2015/19/B/ST7/02494, by Wrocław University of Science and Technology statutory grants and by the Slovak-Polish International Cooperation Program.

References

- [1] L. Hsu i W. Walukiewicz, *Electron mobility in $Al_xGa_{1-x}N/GaN$ heterostructures*, Phys. Rev. B, vol. 56, no 3, pp. 1520–1528, 1997.
- [2] B. Nag, *Electron Transport in Compound Semiconductors*. Berlin: Springer-Verlag, 1980.

ALLOYED OHMIC CONTACTS COMPOSITIONS TO AlGaN/GaN HETEROSTRUCTURES WITHOUT Al

G. Ilgiewicz*, W. Macherzyński, R. Paszkiewicz

Wroclaw University of Science and Technology, Faculty of Microsystem Electronic and Photonics,
Janiszewskiego Street 11/17, 50-370 Wroclaw, Poland

*e-mail: grzegorz.ilgiewicz@pwr.edu.pl

Abstract Ohmic contacts to AlGaN/GaN heterostructures should have ohmic current-voltage characteristic with possibly low contact resistivity. Typically preparation of alloyed ohmic contacts to AlGaN/GaN requires application of Ti/Al/Mo/Au layers and its annealing in temperatures higher than Al melting point. As a result metals from other layers mix with liquid aluminum and conglomerates. There are three ways to avoid the formation of metals' conglomerates: one of them is application of stop-diffusion layers of metals with high melting point and high atomic mass. Other possibility is the preparation of non-alloyed contacts, which preparation do not require of the samples annealing at high temperature. Recently the new method was proposed based on replacing Al with metal layer with melting point higher than the temperature that is required for this metal to form ohmic contact to AlGaN/GaN. To compare the characteristics of the ohmic contact to AlGaN/GaN heterostructures the metallizations containing the Al layer (Ti/Al/Mo/Au) and without Al (Ti/Mo/Au) were fabricated and studied. To compare the surface morphology and contacts properties the SEM images were observed and electrical characteristics of metallic contacts to heterostructure were measured for both types of samples before and after RTA process.

Keywords: alloyed ohmic contact, Al-free, AlGaN/GaN HEMT heterostructures

1. INTRODUCTION

Alloyed ohmic contacts to AlGaN/GaN are usually a composition of metallic layers chosen due to their specific chemical and physical properties useful or required for contact fabrication. The role of the first layer is to extract nitrogen atoms from semiconductor [1,2]. Usually for this purpose the deposition of titanium layers is used. Second component is aluminum and it is responsible for contact resistance. Al oxidate and the high-resistive Al₂O₃ layer forms. To preserve oxidation of Al layer typically gold layer is deposited. Au is highly diffusive metal and, to stop its diffusion into metallization, additional layer is deposited between gold and aluminum [3]. Usually for diffusion stopping layer metals with high molecular mass and high melting point are used, like Nb, Ti and Mo [2]. To form ohmic contact to AlGaN/GaN heterostructure annealing process is required by heating in temperatures higher than Al melting point [4]. But in such conditions other metals dissolves partially in aluminum layer, surface of the contact becomes irregular and that result in the metallization layers discontinuities. Replacing Al with other metal usually result in non ohmic characteristic. It is possible, that other metals are able to form ohmic contact to AlGaN/GaN heterostructures, but they require different temperature and different annealing

time than Al [5]. Aluminum atoms' mobility is higher in annealing temperature than others' metals with higher melting point. To obtain similar atoms diffusivity and reactions possibility, contacts without Al should be alloyed in higher temperatures [6].

2. SAMPLE PREPARATION

Two sample types with different metallization scheme were prepared and tested. The mesa structures were etched in AlGaIn/GaN heterostructures by reactive ion etching in $\text{Cl}_2/\text{BCl}_3/\text{Ar}$ plasma. Before metals' deposition the samples were etched at $\text{HCl}:\text{H}_2\text{O}$ (1:1) solutions. Then, the metallic contacts were deposited by PVD (Physical Vapor Deposition) method using an electron beam evaporator. Ti/Mo/Au and Ti/Al/Mo/Au contacts structures were selected for the study. To check the influence of the annealing conditions on contacts formation Ti/Al/Mo/Au contact were alloyed in 825°C for 60 seconds (Ti/Al/Mo/Au: $230/1000/450/1900\text{\AA}$) or in 900°C for 5 minutes (Ti/Al/Mo/Au: $230/1000/450/1550\text{\AA}$). Samples with Ti/Mo/Au ($230/1000/1550\text{\AA}$) composition were annealed for 60 s in 825°C and then for 5 minutes in 900°C . The annealing process was performed by rapid thermal annealing (RTA) method in nitrogen ambient.

3. RESULTS

SEM images of studied samples after RTA were analyzed (Fig. 1.) to check their morphology. None of them had broken metallizations, although in two cases temperature of alloying was high and annealing time was long.

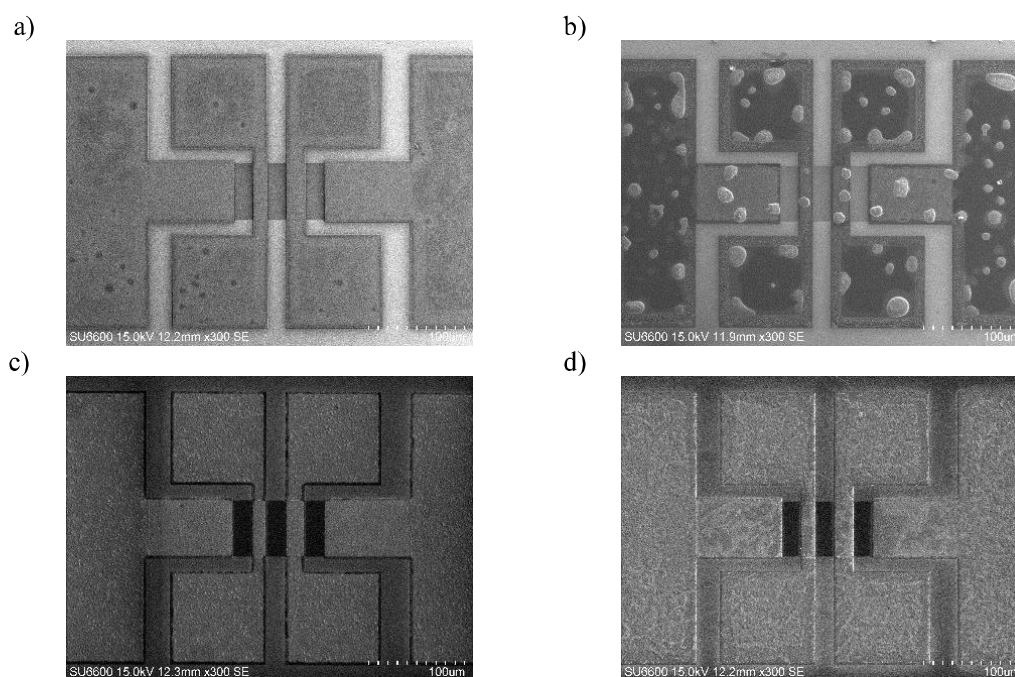


Fig. 1. SEM images of studied structures: a) Ti/Mo/Au after RTA in 825°C for 60 s. b) Ti/Mo/Au after RTA in 825°C for 60 s and 5 minutes in 900°C , c) Ti/Al/Mo/Au after RTA in 900°C for 5 minutes, d) Ti/Al/Mo/Au heated for 60 s in 825°C

The best contact surface was obtained for the samples without Al layer that were annealed for 60 seconds in 825 °C, its morphology was similar to that before RTA process. The same sample additionally heated for 5 minutes in 900 °C had worse surface morphology with randomly distributed hillocks. On contacts edges Au layer had poor adhesion to other metallic layers. This effect was not present after first annealing . Irregularities on contacts containing Al layer were higher for samples that were heated in shorter time and in lower temperature than in sample annealed in longer time and in higher temperature. The electrical parameters of the contact to AlGaIn/GaN after RTA processes are presented in Table 1.

Table 1. Electrical parameters of the contact to AlGaIn/GaN after RTA processes

Metallization	R[Ω/□]	Rc[Ω*mm]
Ti/Mo/Au (RTA: T = 825 °C, t = 60 s)	5.71	non-ohmic
Ti/Mo/Au (RTA: T = 825 °C, t = 60 s + T = 900 °C, t = 300 s)	10159.25	non-ohmic
Ti/Al/Mo/Au (RTA: T = 825 °C, t = 60 s)	2.48	2.00
Ti/Al/Mo/Au (RTA: T = 900 °C, t = 5 min.)	4.55	7.14

It was observed that contact without Al have not had ohmic characteristic (Fig. 2), but Al containing contact annealed in two different conditions have formed ohmic contacts to AlGaIn/GaN heterostructures (Fig. 3).

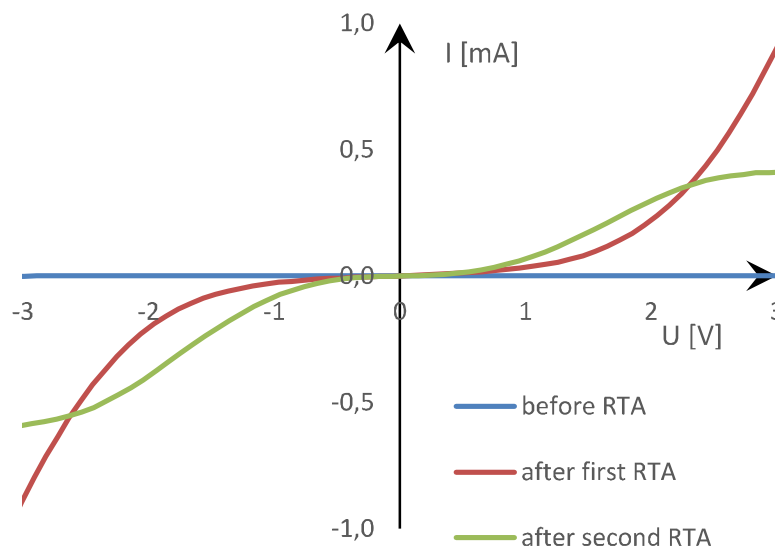


Fig. 2. Current-voltage characteristic of Ti/Mo/Au sample

Al-free contacts before RTA process had very high resistance and had no ohmic characteristic. After first annealing process the contact did not become ohmic. Second RTA process changed characteristic, but they were still not linear.

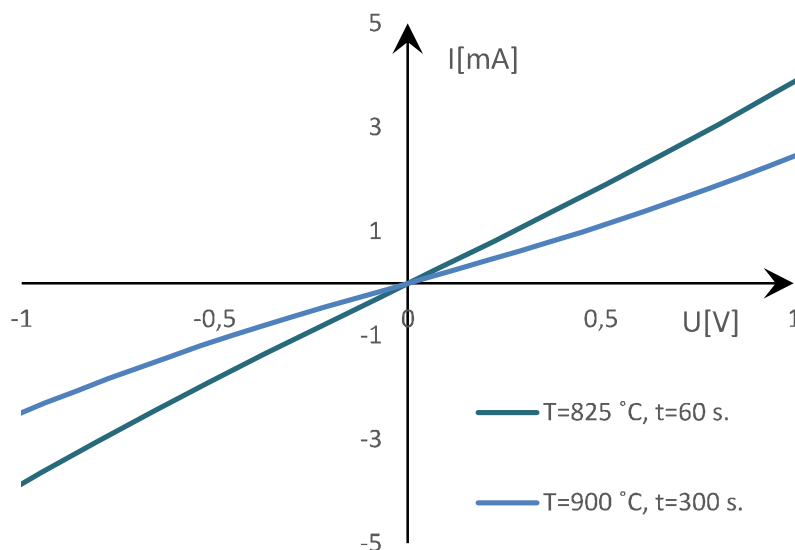


Fig. 3. Current-voltage characteristic for Ti/Al/Mo/Au samples

All Al containing contacts turned out to have ohmic characteristic, but better electrical properties were obtained for samples annealed at lower temperature.

4. CONCLUSION

Al-free contacts had not formed ohmic contact to AlGaIn/GaN heterostructure. It may be the result of annealing in two RTA processes versus annealing in one RTA process, but it also may be the result of too low temperature of alloying process. In Al containing contacts annealing temperature was higher than aluminum melting point. Diffusion in liquids is greater than in solids and more interlayer reactions may occur. But too high temperature and too long heating time could negatively influence contact electrical properties. This phenomenon was observed for example in case of samples with Al layer annealed in 900 °C for 5 minutes. They turned out to have worse electrical parameters ($R=4.55 [\Omega/\square]$, $R_c=7.14 [\Omega \cdot \text{mm}]$) than samples heated for 60 seconds in 825 °C ($R=2.48 [\Omega/\square]$, $R_c=2.00 [\Omega \cdot \text{mm}]$). Annealing in high temperature, although worsened electrical parameters, has a good influence on surface morphology. More irregularities were present on contacts' surface of sample heated shortly in lower temperature. Metals with melting point higher than alloying temperature don't melt, but soluble in liquid aluminum. If RTA process time is short, only small parts soluble and layers congeal with roughness. Long time heating is a reason of the good solubility of other metals in Al. Liquid with no solid on it has flat surface and it stays flat after congelation. It is possible, that in less mixed layers one of metals with lowest resistivity is responsible for sheet resistance. In metallization with mixed layers metal with lowest resistivity is doped with atoms of higher resistant metals. In effect sheet resistance is increased in comparison to pure or less doped metallic layers. To be sure of Al-free contact possibility more research should be done to study contacts properties after RTA processes performed in different temperatures and during different time.

Acknowledgement

This work was co-financed by the European Union within the European Regional Development Fund, through a grant from the Innovative Economy (POIG.01.01.02-00-008/08-05), by the National Centre for Research and Development through the Applied Research Program Grant No. 178782, the program LIDER No. 027/533/L-5/13/NCBR/2014, the National Science Centre under Grant No. DEC-2015/19/B/ST7/02494, by Wroclaw University of Science and Technology statutory grants.

References

- [1] L. Kolaklieva, V. Chitanov, R. Kakanakov, S. Russev, K. Balashev, *Dependence of the Electrical and Morphological Properties on the Ti and Al content in Mo-based Ohmic Contacts for III-V Nitrides*, Proceedings of 28th International Conference on Microelectronics (MIEL 2012), Nis, Serbia, 287-290 (2012).
- [2] B. Van Daele, G. Van Tendeloo, W. Ruythooren, J. Derluyn, M. R. Leys, M. Germain, *The role of Al on Ohmic contact formation on n-type GaN and AlGaN/GaN*, Appl. Phys. Lett. 87, 061905 (2005).
- [3] F. M. Mohammed, L. Wang, I. Adesida, *The role of barrier layer on Ohmic performance of Ti/Al-based contact metallizations on AlGaN/GaN heterostructures*, Journal of Applied Physics 100, 023708 (2006).
- [4] L. Wang, F. M. Mohammed, I. Adesida, *Formation mechanism of Ohmic contacts on AlGaN/GaN heterostructure:Electrical and microstructural characterizations*, Journal of Applied Physics 103, 093516 (2008).
- [5] F. M. Mohammed, L. Wang, H. J. Koo, I. Adesida, *Anatomy-performance correlation in Ti-based contact metallizations on AlGaN/GaN heterostructures*, Journal of Applied Physics 101, 033708 (2007).
- [6] L. Kolaklievaa, V. Chitanov, R. Kakanakov, *Al-free Nanolayered Metallization Systems for Sub-micron HEMTs*, Journal of Nano Research Vol. 17, 203-210 (2012).

LTCC MICROREACTOR UTILIZING DIELECTRIC BARRIER DISCHARGE (DBD)

I. Indyka*, J. Macioszczyk, L. Golonka

Faculty of Microsystem Electronics and Photonics, Wrocław University of Science and Technology,
Janiszewskiego 11/17, 50-372 Wrocław, Poland,
*email: 221090@student.pwr.edu.pl

Abstract Dielectric barrier discharge (DBD) is a discharge occurring between two electrodes covered by dielectric barriers. In this work, a design and fabrication of Low Temperature Cofired Ceramics (LTCC) microreactor for DBD generation is presented. Designed structure consists of eleven layers of a LTCC tape and is divided into two separate elements. Each part is composed of four layers with inner and outer electrodes placed on top and bottom. The inner electrodes are covered with additional layers serving as dielectric barriers. On top of the bottom barrier a discharge chamber is situated. After assembling the structure, it is located between the barriers. A gas inlet is designed in the upper part of the microreactor. In order to examine the influence of various structure parameters on discharge properties, sample structures were created. The samples differed in electrodes size, dielectric barriers thickness, chamber height and width. They were made from KEKO tape. For electrodes, a PdAg conducting paste was used. Vias connecting the inner and outer electrodes were filled with a DP6141 paste. Correct placement of top and bottom parts of the structures is possible due to use of a designed casing. It was created with a 3D printing technique from PCABS.

Keywords: LTCC, microreactor, dielectric barrier discharge (DBD)

1. INTRODUCTION

The use of non-thermal plasmas for many scientific and industrial applications is constantly gaining popularity. Their main advantages are ability to operate at wide pressure range and relatively low temperatures in comparison to thermal plasma [1]. One of ways that allow to achieve such state is creating an electrical discharge. There are several types of discharges that generate non-equilibrium plasma, eq. corona discharge, glow discharge, dielectric barrier discharge [2]. In this work, the latter is brought to attention. Dielectric barrier discharge occurs when at least one electrode is separated from discharge chamber by a dielectric barrier. In order for current to pass an insulating layer, alternating voltages are needed to create the discharge [3]. DBDs have unique features, such as operation at atmospheric pressure, isolation of plasma from electrodes, simple principle of operation, that allow them to be applied in many ways. They are used in ozone generation, surface modification, pollution control, excimer lamps, plasma display panels, analytical chemistry [4-7], biomedical applications [8, 9] and other.

In this work, precursory design of a microreactor which can be used to generate and utilize DBD is presented. For fabrication of the structures, LTCC technology was chosen.

2. MICROREACTOR DESIGN AND FABRICATION

2.1 Structure design

The microreactor structure is made of eleven layers of a LTCC tape as shown in fig. 1. Core elements are a discharge chamber closed by two inner electrodes covered with additional layers. Those layers serve as dielectric barriers. Electrical connection between inner and outer electrodes is established by vias created in layers separating them. In top part of the structure an orifice is placed so that the chamber can be filled with any applied gas. The structure dimensions are 13 mm in width and length, while height is dependent on thickness of LTCC tapes used during fabrication. Discharge chamber length is 11 mm. Gas inlet and outer electrodes diameters are 2 mm each. Vias diameter is 0.2 mm. Remaining parameters are not fixed and depend on values chosen for experiments. For fabrication process the structure was divided into two separate parts (fig. 2): bottom (layers 1-6) and top (layers 7-11). Assembled microreactor is shown in figure 3.

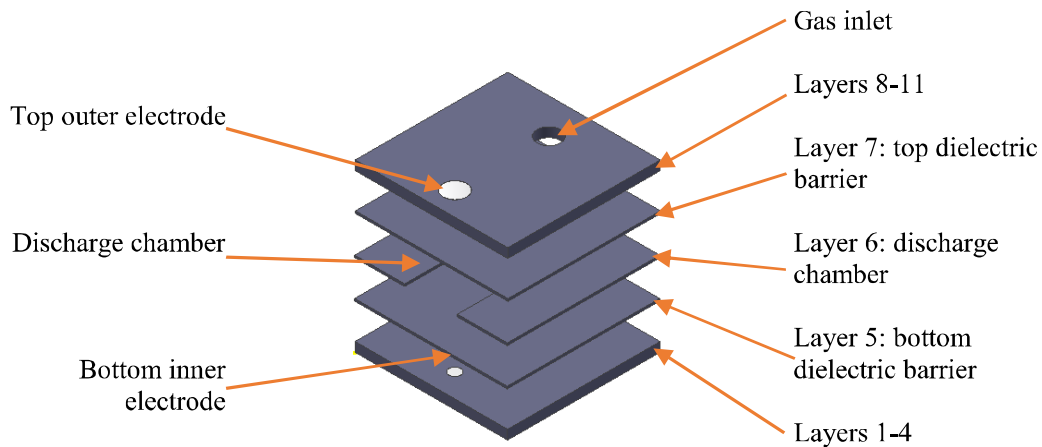


Fig. 1. Layer arrangement of designed microreactor. Bottom outer electrode, top inner electrode and vias between electrodes are not shown in the picture

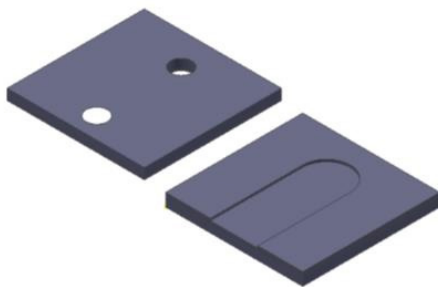


Fig. 2. Two separate parts of the microreactor

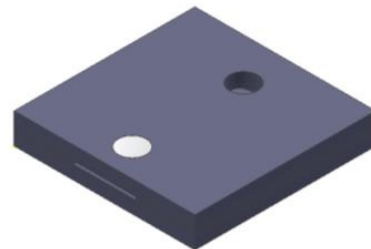


Fig. 3. Assembled microreactor structure

For experimental purposes, sample structures were created with differing parameters. Those parameters were: inner electrodes size, dielectric barriers thickness and chamber height and width. This will allow to determine their influence on discharge properties. Diameters chosen for inner electrodes were 0.5, 1 and 1.5 mm. Chambers widths were 1.5, 3 and 4.5 mm. Barriers thicknesses and chambers heights depend on available thicknesses of LTCC tapes.

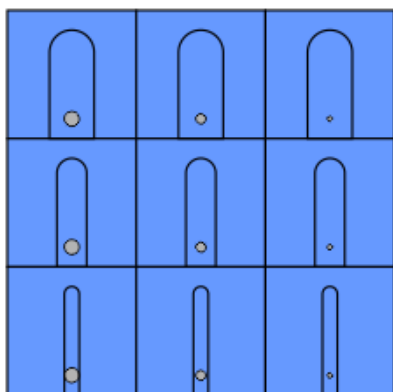


Fig. 4. Configurations of chambers and inner electrodes for nine structures on 50x50 mm section. Electrodes will not be visible after covering with dielectric barriers

Table 1. Configurations of parameters of the samples

Top parts		
	Barrier thickness [μm]	
1.	115	
2.	165	
3.	254	
Bottom parts		
	Barrier thickness [μm]	Chamber height [μm]
1.	115	165
2.	115	254
3.	165	165
4.	254	165
5.	254	254

2.2 Fabrication of samples

KEKO LTCC Tape SK47 [10] was selected for fabrication of the samples. Each sheet of tape was divided into 50x50 mm sections. This way, it was possible to simultaneously fabricate layers for nine separate structures with different electrode size and chamber width configurations (fig. 4). On layers between inner and outer electrodes tape with 254 μm thickness was used, while for remaining layers thicknesses varied between 115, 165 and 254 μm . For tape cutting, a UV laser was used. Lamination of layers was conducted in an isostatic press.

In the first step, sections with vias were cut out from the LTCC tape (layers 1-4 and 8-11). Then vias were filled with conducting paste DP6141. Electrode patterns were deposited on layers 4, 8 (inner electrodes) and 1, 11 (outer electrodes) with screen printer. For this purpose, PdAg conducting paste was used. In the next step, layers 1-4 and 8-11 were laminated. Process parameters were set as recommended in datasheet (21 MPa at 60 °C, 10 minutes). After that, patterns with discharge chambers and dielectric barriers (layers 5-7) were cut out. Then barriers were laminated with previously created laminates using the same parameters as before. Sections with discharge chambers were made from tapes with thicknesses 165 and 254 μm .

Lamination of the latter was conducted in 3.5 MPa at 60°C duration time 15 min. Not used tape parts were removed beforehand. Thinner sections were laminated in higher pressure 15 MPa (at 60 °C, 15 min) and chambers fillings were taken out after the process. In the next step, the laminates were divided into separate structures (fig. 5). The cutting



Fig. 5. Two exemplary laminates before cutting into single structures

was conducted with UV laser. In order to cut through the material, the laminates were cut on both sides. The last step was firing. During this process conducting paste material diffused through dielectric barriers. This effect is not desirable as it can negatively influence DBD generation in fabricated samples. Finished exemplary structures are shown in figure 6.

In total, three sets of top and five sets of bottom elements were created. Just like the sections during fabrication, each set consisted of nine separate structures. Dielectric barrier thicknesses for the covers were 115, 165 and 254 μm . Barrier thickness/chamber height configurations for each set of bottom parts are shown in Table 1.

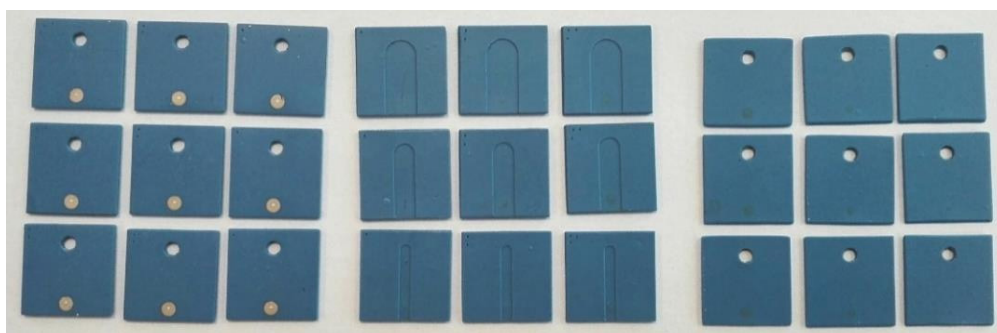


Fig. 6. Finished exemplary structures

3. DESIGN AND FABRICATION OF THE CASING

As mentioned in previous chapter, fabricated microreactor structures were divided into two separate parts. In order to properly generate DBD, it was necessary to correctly position top and bottom elements. For this purpose, a casing was designed. It also enabled easy connection of power supply cables and placement of a gas connector and an SMA 905 optical fiber connector. The casing was designed for 3D printing technology. It was printed with PCABS [11] in 3D printer.

The casing consists of one bottom and two covering parts which can be used interchangeably. In bottom part is located a place for a structure and for an optical fiber connector (fig. 7). A hole and indentation in the space for a structure was designed to place a piece of conducting wire to establish electrical connection with its outer electrodes.

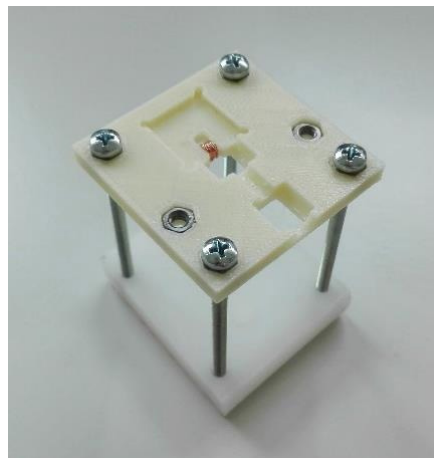


Fig. 7. Bottom part of designed casing for the microreactor structures

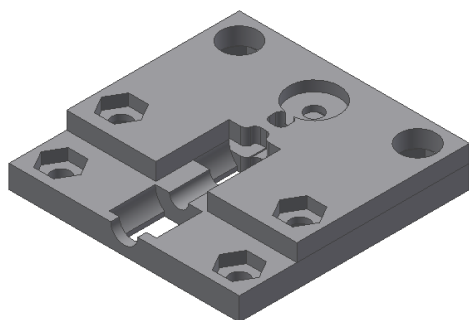


Fig. 8. The casing with multipurpose cover

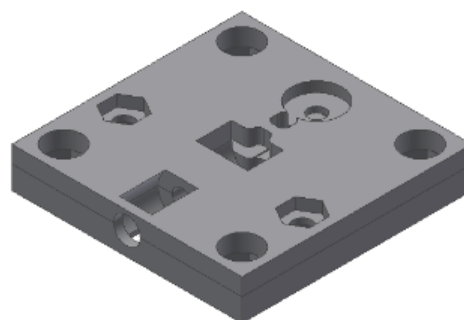


Fig. 9. The casing with the cover for SMA 905 optical fiber connector

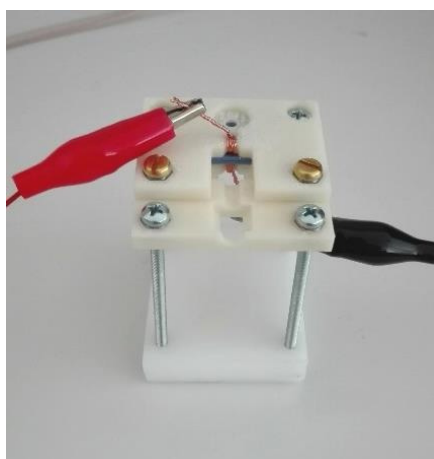


Fig. 10. The casing with mounted microreactor structure and connected power supply cables

First top part was created for multipurpose use (fig. 8) while second top part allows to secure the optical fiber connector (fig. 9). On top of both covers a space for a gas connector is placed. Top and bottom parts can be put together with standard nuts and screws (fig. 10).

4. SUMMARY

To conclude, the DBD microreactor was designed. To examine its performance, eight sets of sample structures with varying parameters were created. The samples were divided into top and bottom parts thus the casing for putting them together was fabricated. In the future, the structures will be tested for proper operation.

References

- [1] A. Fridman, A. Chirokov, A. Gutsol, *Non-thermal atmospheric pressure discharges*, J. Phys. D: Appl. Phys. 38, 1-24 (2005)
- [2] A. Bogaerts et al., *Gas discharge plasmas and their applications*, Spectrochimica Acta Part B 57, 609-658 (2002)
- [3] U. Kogelschatz, *Dielectric-barrier Discharges*, Plasma Chemistry and Plasma Processing 23 (2003)
- [4] C. Meyer et al., *Dielectric barrier discharges in analytical chemistry*, Analyst 136 (2011)
- [5] S. Brandt et al., *Dielectric barrier discharges applied for optical spectrometry*, Spectrochimica Acta Part B 123, 6-32 (2016)
- [6] S. Brandt et al., *Dielectric barrier discharges applied for soft ionization*, Analytica Chimica Acta 951, 16-31 (2017)
- [7] O. Goossens et al., *Application of atmospheric pressure dielectric barrier discharges*, Surface and Coatings Technology 142-144, 474-481 (2001)
- [8] N. Bibinov et al., *Basic and Biomedical Applications of Dielectric Barrier Discharge (DBD)*, Biomedical Engineering Trends in Materials Science, InTech (2011)
- [9] B. Boekema et al., *A new flexible DBD device for treating infected wounds*, J. Phys. D: Appl. Phys. 49 (2016)
- [10] Datasheet, KEKO LTCC Tape SK47 (2017)
- [11] Material Data Sheet: Z-PCABS (2016)

DATA MINING TO POWER QUALITY ISSUES

M. Jasiński

Faculty of Electrical Engineering, Wrocław University of Science and Technology,
Wybrzeże Wyspińskiego 27, 50-370 Wrocław, Poland
e-mail: michal.jasinski@pwr.edu.pl

Abstract *The electricity is an essential part of everyday life. Our world would not exist in such form without it. Present attitude to energy is not only about its attendance, but to assure the high level of it. Power quality assessment become more and more popular. The basic assessment depend on agreement of parameters with standards and country regulations. Although, detail analysis of power quality cannot consist only on agreement with standards and country regulations. Term of analysis should be longer than typical 1-week analysis of typical working conditions of electrical power network. Such analysis are related with huge amount of data and additional tools should be consider to support the assessment of power quality. Author suggest using data mining techniques as a solution for power quality data analysis. This paper contain the description of data mining techniques and reasons why and when it should be use to power quality analysis.*

Keywords: power quality, data mining, clustering, smart grids

1. INTRODUCTION

The approach to electric energy has changed over the years. Present attitude to energy is not only about its attendance, but to assure the high level of it. Due to this assessment of power quality (PQ) become essential part of everyday life [6]. The basic assessment depend on agreement of parameters with regulations and standards. Main European standard is [2], IEEE standard [5], and country regulation e.g. in Poland [10].

Power quality data analysis typically consist of agreement of parameters in selected representative 1-week data. Such analysis are required due to standards and regulations, but are not enough sufficient if the knowledge about selected part of electrical power network is needed. Due to this the long power quality data should be take into consideration. Each week of power quality monitoring create a set of 1008 10-minute data for each parameter.[9] Following parameter may be take into analysis:

- frequency level,
- voltage level,
- voltage unbalance,
- voltage fluctuation,
- harmonic content: Total Harmonic Distortion (THDu), content of each harmonic from 2nd to 50th.

Due to this the global long term power quality data analysis require a tool to support it. Data mining techniques seems to be used for PQ data.

2. DATA MINING

Data mining is stated by a lot of definitions. Definition for power quality issues may be this presented in [4]: “Data mining is the analysis of (often large) observational data sets to find unsuspected relationships and to summarize the data in novel ways that are both understandable and useful to the data owner”.

Literature points a lot of data mining techniques classification. In this article classification given by CIGRE (Council on Large Electric Systems) and according to supervision are presented. Figure 1 presents the classification according to [1] and figure 2 like in [3].

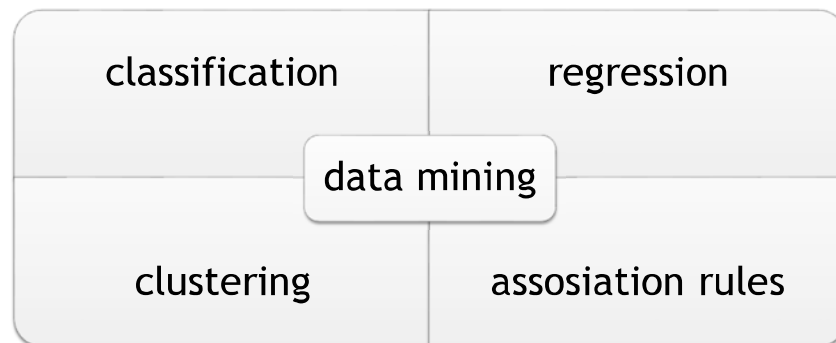


Fig. 1. Data mining techniques according to [1]

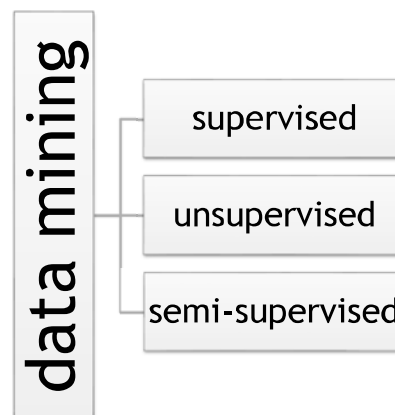


Fig. 2. Data mining techniques according to supervision

There's a lot of pros of data mining appliance to any huge data bases e.g. [8]:

- reduction of huge amount of data to few basic categories,
- achievement of uniform group and their essential characteristic,
- achievement of classification of work condition of analyzing object,
- achievement of the division into groups as the element of analysis connected due to the characteristics data.

3. DATA MINING APPLIANCE TO POWER QUALITY DATA

Data mining techniques may be useful for power quality data especially if the time of measurement is longer than 1 week or the measurements are multipoint. Appliance the data mining assure a classification which represents typical and untypical data. So it's possible to define states of working for each electrical power network of each company.

Example of data mining techniques which find the appliance to power quality data may by clustering. Cluster analysis gives different groups of data. Usually, one or more group have data which represents „bad” quality, e.g. data which contain voltage events. Analysis of „bad” quality time may lead to achieve a knowledge of which device or machine is working incorrectly and also adverse working conditions.

Additionally analysis of power quality level, especially elimination of “bad” energy time may assure:

- reduction of energy consumption (i.e. assure the correct measure of energy counter),
- increase continuity of supply (i.e. reduction of overheating the cable),
- increase continuous of production process (i.e. reduction of damage of crucial electric and electronic devices). The received manuscripts will be reviewed by the editors and then by the Scientific Committee. The editors kindly asks the authors to follow the presented guidelines.

Example of appliance clustering to power quality data may be presented in [7]. This is a case-study of using clustering with k-mean algorithm, Chebyshev distance, with 2 cluster as a set value. It appointed two clusters. Cluster 1 consist of all data which should be taken into classic assessment of power quality. Cluster 2 consist of data which contain voltage events. Voltage events cannot be taken into analysis of power quality level so cluster analysis assure the possibility of automatization of flagging process which is first step of each PQ assessment.

4. SUMMARY

Power quality analysis are essential for each branch of industry. Electronic engineer should be conscious of PQ problem because a lot of devices and machines which they use during they everyday work influence on power quality level. Such devices are: electric furnace, welding machine, microwave devices, laser.

It's important to be conscious that, single device does not lead to huge power quality problems but when the number is increasing the scale of problem is increasing. Present and future industrial plants or laboratories may take into consideration power quality issues to assure their continuous working.

This article present the need of using data mining techniques to support power quality analysis, but this tools may be useful in other situations where there's a lot of data.

The changing of electrical power network is connected with smart grids which consist of huge amount of data so this tools will be an important part of nearest future.

References

- [1] CIGRE Brochure 292, *Data mining techniques and applications in the power transmission field*, CIGRE, (2006)
- [2] EN 50160: *Voltage characteristics of electricity supplied by public distribution network*.
- [3] Han J., Kamber M., *Data Mining: Concepts and Techniques*, Second Edition, http://ccs1.hnue.edu.vn/hungtd/DM2012/DataMining_BOOK.pdf
- [4] Hand D., Mannila H., Smyth P., *Principles of Data Mining*, MIT Press, Cambridge, MA 2001
- [5] IEEE Std. 1159: *Recommended practice on monitoring electric Power quality*
- [6] M. Jasiński, *Comments on the influence of power quality on the performance of electric and electronic devices*, Photonics and Microsystems: proceedings of 2016 International Students and Young Scientists Workshop : Szklarska Poręba, Poland, 28-30 October 2016 / [eds. Sergiusz Patela, Wojciech Kijaszek, Dariusz Przybylski]. Wrocław : Wydawnictwo Gmork, 38-42 (2017).
- [7] M. Jasiński, T. Sikorski, *Celowość stosowania analizy skupień do oceny zagadnień związanych z jakością energii elektrycznej w sieciach kopalnianych*, „Zeszyty Naukowe Uczelni Jana Wyżykowskiego. Studia z Nauk Technicznych” 2017, in Polish, in press
- [8] M. Jasiński, T. Sikorski, J. Karpiński, M. Zenger, *Long term power quality data*, Electrical Power Networks 2016, EPNet 2016 : Scientific-Technical Conference, 19-21.09.2016, Szklarska Poręba, Poland. Danvers MA : IEEE, pp. 1-6. (2016)
- [9] A. Klajn, M. Bątkiewicz-Pantuła, *Application Note – Standard EN 50 160 : Voltage characteristics of electricity supplied by public electricity networks*. [Brussels]: European Copper Institute, (2013)
- [10] Rozporządzenie Ministra Gospodarki z dnia 4 maja 2007 r. w sprawie szczegółowych warunków funkcjonowania systemu elektroenergetycznego, ze zmianami 21 sierpnia 2008 r. (Dz.U. 2008 nr 162 poz. 1005), in Polish (2008)

INFLUENCE OF AVERAGE MOLAR MASS OF POLYETHYLENIMINE ON GOLD NANOPARTICLES SYNTHESIS

E. Kuc^{1,*}, O. Rac-Rumijowska¹, M. Fiedot-Toboła¹, E. Sasiadek², H. Teterycz¹

¹Faculty of Microsystem Electronics and Photonics, Wrocław University of Science and Technology, Janiszewskiego 11/17, 50-372 Wrocław, Poland

²Faculty of Electrical Engineering, Wrocław University of Science and Technology, Wybrzeże Wyspińskiego 27, 50-370 Wrocław, Poland

*e-mail: 212565@student.pwr.edu.pl

Abstract *Method of synthesis of gold nanoparticles (AuNPs) using chemical method has been presented in this publication. AuNPs were measured using UV-Vis spectroscopy and dynamic light scattering (DLS) methods. Phenomena of surface plasmon resonance (SPR) have been observed in spectroscopic measurements, which allows to determine the size of obtained nanoparticles. Polyethyleneimine (PEI) was used as a nanoparticle stabilizing agent. The influence of the molecular mass of the stabilizing agent on the synthesis time and size of gold particles was investigated.*

Keywords: optoelectronics, photonics, microsystems

1. INTRODUCTION

Nanoparticles are structures in the size range of 1 to 100 nm. They have different physical, chemical and biological properties that their bulk forms. It is caused by a high surface to volume ratio, which is increasing with smaller particles diameter. This causes an increase in nanoparticle activity and effects on the absorption and reactivity properties of the particles. The reduced size causes change in the total energy that is responsible for thermodynamic stability. This is a result from disturbances in the wave function of the electrons. For comparison, the bulk silver melts at 960°C and silver nanoparticles of 2.4 nm have a melting point of 360°C [1]. Changes are also observed in physical properties of materials such as thermal, electrical and magnetic conductivity. Metal nanoparticles are a group of materials with potentially the widest range of applications. Their properties clearly depend on the shape of the structure. When the surface is more developed has more significant impact on chemical and antimicrobial activity or adsorption properties. Nanoparticles are widely used in many fields such as medicine, pharmaceuticals, cosmetology, dentistry, photography, construction materials and explosives materials [1].

2. EXPERIMENTAL PART

Gold nanoparticles (AuNPs) were obtained by chemical reduction of gold ions. As a gold ions precursor water solution of chloroauric acid (HAuCl₄) of concentration 0.08 mol/dm³ from POCH company was used. As stabilizers 1 mol/dm³ polyethyleneimine (PEI) (Sigma Aldrich) was used. Four types of PEI with different average molecular weight were used: 2 kDa, 25 kDa, 750 kDa and high molecular weight.

All synthesis were carried out at room temperature in water environment at a constant volume of 100 ml. Concentration of gold nanoparticles was 100 ppm. During the reduction reaction of gold ions solutions were mixed on a magnetic stirrer at a rotational speed of 500 rpm. During the synthesis to the water 0.4 ml of PEI was added, stirred for 2 min and then added with 0.312 ml of chloroauric acid.

The presence of gold nanoparticles in solutions was investigated by using the Shimadzu UV-1800 spectrophotometer. The absorption spectrum was measured in the range of 190 nm to 800 nm. The size distribution of the obtained gold nanoparticles was determined by dynamic light scattering (DLS) method. For this purpose, the Nicomp 380ZLS (Particle Sizing Systems, USA) was used, which included a laser with a wavelength of 532 nm (50 mW). To determine pH of colloids Elmetron CPO-501 pH-meter was used.

3. RESULTS AND DISCUSSION

3.1 UV-Vis absorption

Results of spectrophotometric analysis in the UV-Vis range confirmed the presence of gold nanoparticles in all samples. On the absorption spectra in samples stabilising by PEI with different average molecular mass characteristic peak about 520 nm is observed [2].

The kinetics of the formation of AuNPs with different stabilising agents was evaluated. The differences in gold nanoparticles formation are due to the using different molecular mass of polyethyleneimine. Peak at a wavelength about 350 nm can indicate the formation of complexes between gold particles or ions and polymer macromolecules, which are formed before the crystallization nuclei reach a critical size to obtain stable nanoparticles [2]. This reduction reaction does not require an additional reducing agent. However, nanoparticles are formed really slowly.

In the case of PEI Mw 2 kDa, the gold ion reduction process started after about 50 min, was intense for about 24 h and after about 6 days was ended. The sample remained stable for a further period of time (Fig. 1a, e). For 25 kDa PEI the reaction started the latest, after about 8 h (Fig. 1b, e) and the absorption varied over the next three weeks. In the case of PEI 750 kDa, the absorption increased at a similar time as for PEI 2 kD and after 20 days it stabilized at the same level (Fig. 1c, e). Synthesis in the presence of high molecular weight PEI began after 2 h and occurred slowly over a week (Fig. 1d, e). Changes in the absorption spectra were also observed visually - the color of the samples varied from yellow to pink and burgundy.

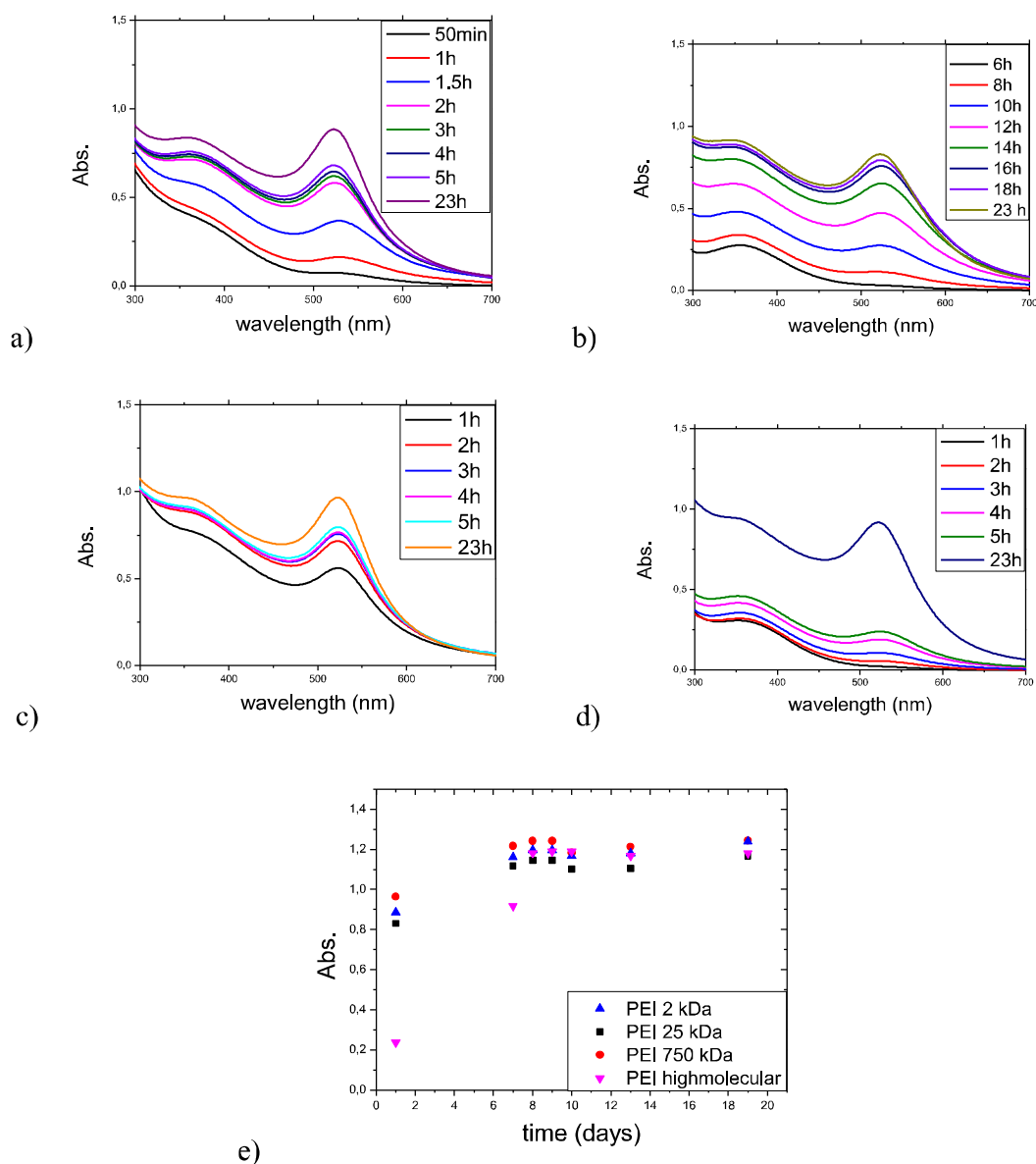


Fig. 1. UV-Vis absorption spectra of gold colloids stabilising by: a) PEI 2 kDa, b) PEI 25 kDa
c) PEI 750 kDa, d) highmolecular PEI, e) changes in absorbance over time

3.2 pH of gold colloids

The pH value were also measured for the tested samples (Tab. 1). For PEI 2 kDa the pH was 5.8 and for the slowest synthesis with PEI 25 kDa the pH was highest and was 6.1. The lowest pH of 4.1 was observed for colloids stabilized with the highest molecular weight polymers.

Table 1. pH of gold colloids with different molecular weight of stabilizing agent

PEI	pH
2 kDa	5.8
25 kDa	6.1
750 kDa	4.1
highmolecular	4.1

3.3 DLS measurements

The size distribution of the obtained gold nanoparticles was determined by dynamic light scattering (DLS) method (Fig. 2). AuNPs stabilised by PEI 2 kDa have 3.2 nm (99.7%). Other 0.3 % have 53.7 nm. The resulting particles are monodisperse. Gold nanoparticles synthesized in the presence of PEI 25 kDa have an average size 29.7 nm (91.4%) and the remaining 8.6% was 167.8 nm. Colloid containing PEI 750 kDa consist AuNPs with diameter 2.5 nm (90.5 %), 9% of AuNPs have 7.3 nm and 0.3% 45.2 nm. In the last sample with highmolecular PEI, the average size of AuNPs is 5.9 nm in 95.3%. 4.3% of nanoparticles have diameter 39.7 nm and 0.4% have 217 nm.

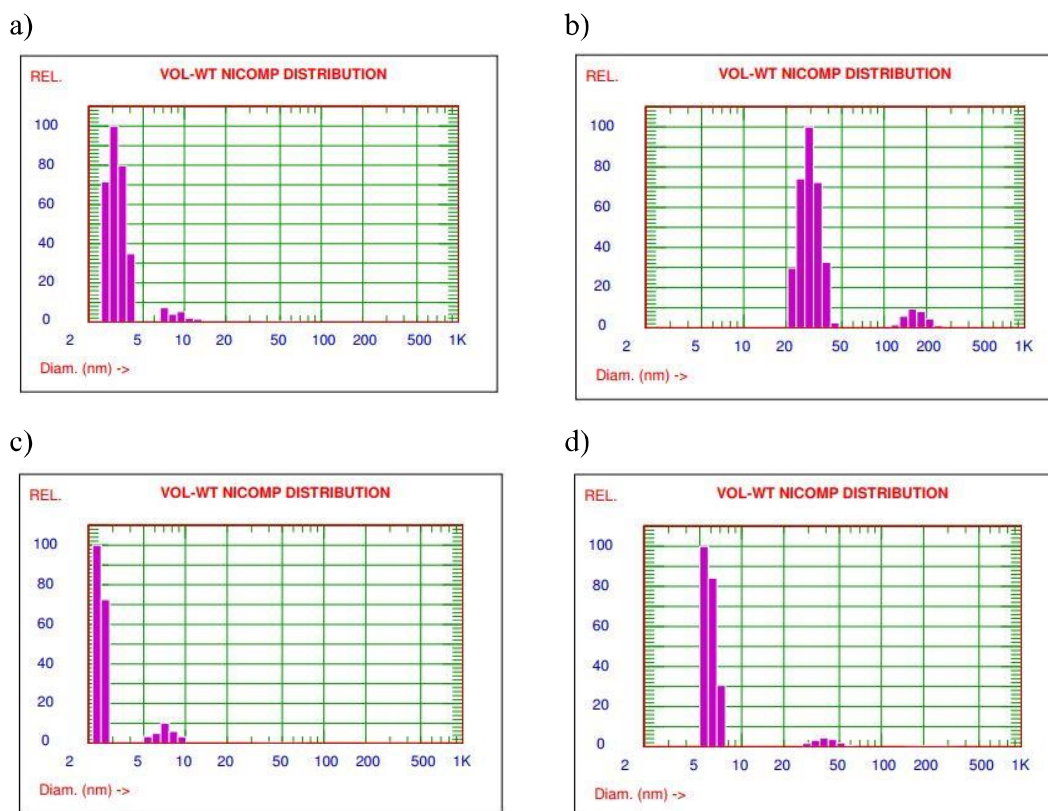


Fig. 2. Size of gold nanoparticles measure by DLS method: a) PEI 2 kDa, b) PEI 25 kDa, c) PEI 750 kDa kDa, d) PEI highmolecular

Nanoparticles obtained in the presence of polymer with the lowest molecular weight are produced most rapidly. This is related to the easier migration of ions into the solution. Fast motion of gold ions allow to the formation of more nucleation centers, resulting in small particles and monodisperse particle size distribution. For this reason, strong reducers are often used in nanoparticle synthesis to permit a significant acceleration of particle formation.

The largest particles were obtained in the synthesis conducted in the presence of PEI Mw 25 kDa, where the synthesis started after 6 h. The influence on particle size have also the pH of the solutions, where in the colloid with PEI 25 kDa the pH is highest in relation to the other samples and is 6.1.

Mohammed et al. for the synthesis of gold nanoparticles was used as stabilizer PEI Mw 600 Da. Syntheses were made without a reducing agent and with a reducing agent in the form of sodium borohydride [3]. The synthesis was carried out without sodium borohydride lasted 2 weeks, where the solution gradually changed its colour. In the synthesis with reducing agents the synthesis took place within 15 min, where the clear solution changed colour to brown, which confirmed the presence of gold nanoparticles. In this studies, attention was also paid to the effect of pH on the particle synthesis mechanism. It has also been noted that lower pH promotes faster reduction of gold precursor and formation of smaller particles. In our results also the synthesis is faster at low pH than high.

4. SUMMARY

This article presents the synthesis of gold nanoparticles in solution without reducing agent. In the literature, examples of obtaining gold nanoparticles stabilized with polyethyleneimine both with and without reducing agent are available, but usually they only refer to one type of polymer. This publication is a compilation of the results obtained for the synthesis nanoparticles having different molecular weights stabilized by polyethyleneimine. As can be observed, average molecular mass has a great influence on both the synthesis time and the particle size. This paper will allow to select the optimum polymer for gold synthesis for specific applications.

Acknowledgement

This work was founded from Funds for Science by Faculty of Microsystem Electronics and Photonics, Wrocław University of Science and Technology (statutory activity).

References

- [1] Katedra Technologii Środowiska, Wydział Chemii, UG, „Otrzymywanie nanocząstek złota, srebra i miedzi metodą redukcji chemicznej”, aktualizacja 29.09.2015 r.
- [2] Hecold, Mateusz, et al. "The Effect of PEI and PVP-Stabilized Gold Nanoparticles on Equine Platelets Activation: Potential Application in Equine Regenerative Medicine." *Journal of Nanomaterials* 2017 (2017).
- [3] Mohammed, Fiaz S., Scott R. Cole, and Christopher L. Kitchens. "Synthesis and enhanced colloidal stability of cationic gold nanoparticles using polyethyleneimine and carbon dioxide." *ACS Sustainable Chemistry & Engineering* 1.7 (2013): 826-832.

- [4] Wen, Shihui, et al. "Synthesis of polyethyleneimine-stabilized gold nanoparticles for colorimetric sensing of heparin." *Colloids and Surfaces A: Physicochemical and Engineering Aspects* 419 (2013): 80-86.
- [5] Malina, Dagmara, et al. "Otrzymywanie nanocząstek metali w polu promieniowania mikrofalowego z zastosowaniem wybranych substancji redukująco-stabilizujących." *Infrastruktura i Ekologia Terenów Wiejskich* (2017).

ENCAPSULATED QUANTUM DOTS AS BIOCOMPATIBLE IMAGING AGENTS FOR CANCER DIAGNOSIS

K. C. Nawrot*, M. Nyk

Advanced Materials Engineering and Modelling Group,
Faculty of Chemistry, Wrocław University of Science and Technology,
Wybrzeże Wyspiańskiego 27, 50-370 Wrocław, Poland
*e-mail: katarzyna.c.nawrot@gmail.com

Abstract *Near-infrared (NIR) optical imaging technique within the 'biological transmission window' provides a non-invasive real-time monitoring for cancer diagnosis. Currently, quantum dots attract more and more attention as bioimaging agents due to their excellent optical properties, however, most of them are toxic, hydrophobic and incapable of linking to biomolecules. These disadvantages may be overcome by encapsulation in micelles, nanoparticles and polymeric pseudophases.*

Keywords: quantum dots, bioimaging tracking, encapsulation, nanocapsules, micelles

1. INTRODUCTION

Along with cardiovascular diseases, respiratory diseases and diabetes, cancer is one of the leading death cause [1]. In 2015, it contributed to about 8.8 million of deaths globally. In low- and middle-income countries, a larger part of population dies because of cancer than due to malaria, HIV/AIDS and tuberculosis together [2]. Effective treatment possibility is dependent on the detection stage so a sensitive method for screening is extremely needful. Cancer diagnosis is performed by laboratory tests of blood or urine detecting abnormal levels of certain biomarkers, by different imaging procedures or by biopsy through a fine needle, a wider coring needle or an open surgical incision. Laboratory tests are inaccurate and may show either falsely negative or positive results. Biopsy is considered as the most accurate method. Open surgical incision is even treated as the diagnosis standard, however, it is highly invasive. Generally, biopsy should not be treated as the first step of cancer detection. Less invasive biopsy techniques are less accurate [3]. Bioimaging, with its ability to provide metabolic, functional, morphological and structural information [4], seems to be promising and may reduce the need for invasive penetrations into bodies.

The bioimaging methods commonly used nowadays are ultrasounds, X-ray, computerized tomography, radiography, positron emission tomography and magnetic resonance imaging. However, they are insensitive, non-specific and expose patients to radiation. In contrast, optical imaging techniques appear to be non-invasive and provide real-time monitoring with high resolution. These approaches should be performed within the wavelength range which provides possibly minimal background interferences and allows deep tissue penetration [5]. The near-infrared fluorescence imaging (within the 'biological transmission window' [6]: 650-1000 nm) is a promising technique as it ensures low absorption and autofluorescence from tissues and biological substances. At shorter wavelengths, the major tissue chromophores exhibit significantly higher absorption whereas above 1000 nm the absorption by water interferes imaging unacceptably [7].

Moreover, to obtain a clear, long-lasting image a suitable NIR agent is necessary. Both organic and inorganic substances may be used in bioimaging. Traditionally used organic dyes may easily conjugate with wide range of specific biomolecules and be produced on large scale [5]. However, they are optically unstable, not resistant to photobleaching and are required high dosage to achieve sufficient signal-to-noise ratio [8]. Inorganic agents are mainly quantum dots (QDs) but QDs, which are the most frequently used in bioimaging, display high toxicity as they contain cadmium. Also, they are hydrophobic so they aggregate in biological fluids and possess no functional groups which could bind to biomolecules [6]. However, in contrast to organic dyes, they display high brightness and photostability. They are characterized by longer photoluminescence lifetime and higher quantum yields [9]. They are suitable for NIR imaging and the colour of light they emit may be modified by changing their size [8]. With a high power short laser pulse excitation semiconducting QDs are also able to simultaneously absorb two or more photons of lower energy than the band gap producing a photon of higher fluorescence energy. This opens a possibility for QDs to be used as markers for 3D multiphoton microscopy which enables imaging deep into the sample and also with less overall photobleaching.

There exist several methods leading to transfer QDs into aqueous solution, provide linking with biomolecules and reduce their toxic impact on diagnosed organisms. The surface of imaging particles may be modified by adding hydrophilic groups. However, it may reduce quantum efficiency and the possibility to control ligand exchange reactions is usually limited [6]. Another group of methods is amphiphilic polymer coatings formation, e.g. by silanization, but the particles obtained during this process have usually low quantum yield and low concentrations [10]. Encapsulation seems to be a promising method as it does not cause surface alteration maintaining the optical properties of QDs. Moreover, in micelles, nonspecific adsorption is inhibited due to the high density of the systems' surfaces [11].

This paper is intended to present and explain the unique QDs' properties which made them excellent candidates for using as imaging agents in cancer diagnosis. In order to overcome biocompatibility, QDs require a technology providing a suitable surface modification without undesirable alteration of their optical properties and encapsulation methods seems to be the most promising. In this work, encapsulation possibilities are briefly reviewed.

2. QUANTUM DOTS AND BIOIMAGING

Quantum dots are semiconductor nanocrystals with diameters of the same size or smaller than the excitation Bohr radius. The mobility of their electrons and holes is limited being the reason of their unique electronic properties [12]. As semiconductors, they typically contain elements from the periodic groups 12 and 16 or 13 and 15 [12] but also different combinations may be found in the literature, especially because QDs are not necessary simple chemical compounds but they may be core type, core-shell type or alloyed type.

2.1 Quantum dots types

QDs which are simple components are called core type. Popular core type QDs are chalcogenides of metals from the periodic group 12, e.g. CdTe, ZnS, CdSe. The properties of these nanocrystals, such as the colour they emit, may be modified simply by changing their size (Fig. 1). A decrease in the particle diameter results in the increase of energy

difference between the lowest conduction band and the highest valence band. Therefore, smaller particles require more energy to be excited but they also release more energy when returning to the ground state, emitting colour of a shorter wavelength.

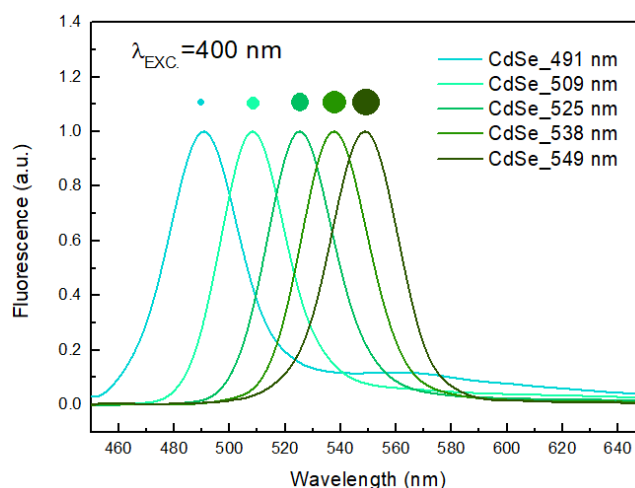


Fig. 1. Dependence between size of QD and wavelength of the emitted light (by the example of CdSe QDs)

However, charge carriers may recombine without photon release reducing quantum yield. Thus, light generation efficiency is reduced. Core type quantum dots are hardly ever used for bioimaging and are replaced by core-shell nanocrystals. The upgraded QDs are tiny particles of one material embedded in shells of another semiconductor with a wider band gap; in bioimaging cadmium-based are popular: CdSe-ZnS, CdTe-CdSe, CdTe-ZnS [6]. Their efficiency and brightness is ameliorated in comparison to core type nanocrystals.

The possibility to change the wavelength emitted by nanocrystals by modifying their size is a chance for simultaneous observation of multiple QDs within the same organism [8]. But the diameter of the particles intended to be used in human organism as imaging agents or as a part of theranostic system is sometimes restricted. Therefore, a way to modify optical properties of QDs without changing their sizes was developed in form of alloyed semiconducting nanoparticles. They are multicomponent QDs which photo-properties are dependent on the proportion of different atoms in the structure, e.g. CdSe_xTe_{1-x} [13].

2.2 Optical properties of QDs and bioimaging

An ideal bioimaging agent should emit in a narrow, simply-tunable emission spectrum but absorb in a wide spectrum, have high quantum yield and be resistant to photobleaching and chemical degradation in order to show the image for a long time [9]. These properties may be achieved with QDs making them superior to organic dyes for application in bioimaging. The tunability of emission spectrum allows to use QDs within the biological transmission window and enables multi-colour tracking. The high quantum yield of QDs comes from their large molar extinction coefficients: 10-50 larger than organic agents. They were reported to be 10-20 times brighter [14]. Also, the resistance to photobleaching enables sensitive and long-time detection [12].

However, bioimaging agents must display biocompatibility: lack of toxicity, solubility in biological liquids (hydrophilicity) and ability to link to biomolecules. Raw QDs do not fulfill these requirements as they typically contain toxic Cd, Se, Te, Hg or Pb [9] and have hydrophobic surface with no functional groups which could bind to biomolecules.

Several studies proved that QDs containing cadmium are toxic and elimination of remaining potential reasons suggested that the main factor causing cytotoxicity are free Cd^{2+} ions [15, 16, 17] so elimination of their negative impact is crucial. Moreover, modification of QDs to make them hydrophilic is essential for biological application because it allows them to travel through biological liquids by protecting them from aggregation and precipitation. Finally, the effectiveness of cancer detection is dependent on the ability of imaging agents to 'find' mutated cells by penetrating their membranes or by binding to specific substances which appear in case of cancer. QDs have to be suitably modified to possess this ability.

3. QUANTUM DOTS ENCAPSULATION

Biocompatibility of QDs may be increased by surface engineering, polymer coating or encapsulation. As it was mentioned, the third solution is the most promising as it does not cause alteration of QDs' physico-chemical properties while e.g. ligand exchange reactions are difficult to control producing less stable particles. QDs may be encapsulated in polymer pseudophases, in nanoparticles or in micellar systems [6].

Polymer-based nanocarriers enable facile modification to obtain multifunctional and targeted delivery, provide high structural stability and high encapsulation efficiency [18]. A very promising material for QDs encapsulation is chitosan. Its cationic charge and hydrophilicity stabilize semiconducting nanocrystals in the biological liquids. Chitosan may ease targeting tumour cells via binding with folic acid/galactose because these compounds are taken more willingly by mutated cells [19]. A successful synthesis of water-dispersed ZnO-QD-chitosan-folate carrier for anti-cancer drug delivery was reported [19].

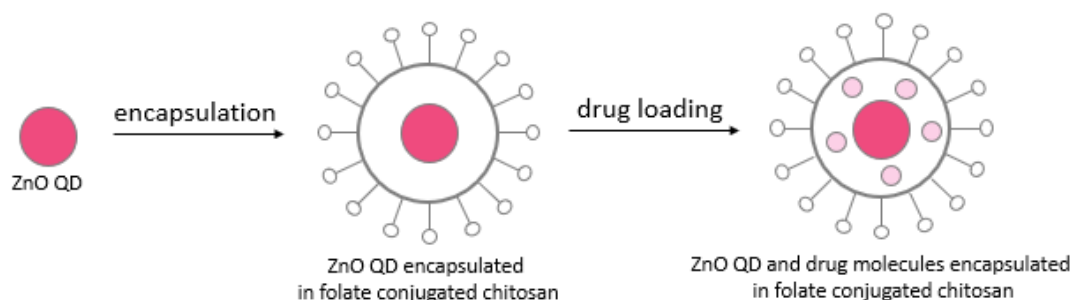


Fig. 2. Preparation of ZnO-QD/drug-loaded chitosan-folate carrier [19]

The most frequently used nanoparticles are made from poly(alkylcyanoacrylate) (PACA) or poly(lactic-co-glycolic acid) (PLGA) due to their biocompatibility and biodegradability. PACA nanoparticles were reported to facilitate transport of drugs through blood-brain barrier, overcome drug resistance in tumour cells and allow skin penetration of drugs. Also, poly(butylcyanoacrylate)-embedded CdSe/CdS core-shell QDs with great fluorescent properties were synthesised so that this polymer may serve as a carrier for therapeutic and

diagnostic systems [20]. In another study [21], CdTe/CdSe QDs were encapsulated in PLGA. The obtained nanospheres were characterized by hydrophilicity, low cytotoxicity, high cellular uptake, stability, sufficient circulation times and sensitivity.

Therapeutic and diagnostic properties were also obtained by Bai et al. [18] through preparation of QD/gene-loaded nanocapsules made from multifunctional amphiphilic polymer together with polyethylene glycol – poly(lactic-co-glycolic) acid. QDs emitted red light whereas pDNA expressed green fluorescence protein so simultaneous tracking of the nanocapsules delivery in cells and gene transfection efficacy was possible.

An interesting combination of theranostic features exhibited by QD/drug-loaded nanoparticles was demonstrated by Huang et al. [22]. They prepared a pH-responsive nanocapsules of poly(amino acid) functionalized with oleyamine loaded with a hydrophobic anticancer drug and Ag₂S QDs together. These systems provided real-time tracking and nontoxicity to cells till the drug release in acidic lysosomes of cancer cells.

The nanocarriers may also be in the form of micelles. Szeremeta et al. [23] prepared CdSe_xTe_{1-x} QD-doped Brij 58® micelles with luminescent properties within the biological transmission window, with high quantum yield, sharp emission spectra, stability. The emission maximum of the doped micelles displayed a 60 nm blue-shift in comparison to raw QDs, however, it was still not excluded from the biological transmission window.

4. CONCLUSION

Due to their size and composition, QDs exhibit unique optical properties such as tunability and narrowness of absorption and emission spectrum, high quantum yield and resistance to photobleaching. For bioimaging application, they have to be modified to reduce their toxicity, increase their hydrophilicity and ability to bind with biomolecules. All of these features may be achieved by encapsulation in form of hydrophobic pseudophases, in nanoparticles or in micelles. Successful and efficient encapsulation was performed within chitosan, PACA, PLGA, functionalized poly(amino acid), Brij® and other materials which provided enhanced cancer-targeting properties, water solubility, biodegradability while maintaining optical properties of QDs. An important new direction for nanomedicine is the use of nanoplatforms called ‘theranostics agents’ which combine therapeutic and diagnostic functionalities. Thus, preparation of multi-functional carriers by encapsulation of bioimaging QDs along with anti-cancer drugs and other therapeutics is a popular practice.

References

- [1] Global action plan for the prevention and control of noncommunicable diseases [website]. Geneva: WHO; 2013
- [2] Global health observatory: the data repository [website]. Geneva: WHO; 2017
- [3] Kasraeian S., Allison D.C., Ahlmann E.R., Fedenko A.N., Menendez L.R., *Clin Orthop Relat R* 468, 2992-3002 (2010)
- [4] L. Fass, *Mol Oncol* 2, 115-152 (2008)
- [5] S. Luo, E. Zhang, Y. Su, T. Cheng, C. Shi, *Biomaterials* 32, 7127-7138 (2011)
- [6] U. Bazylińska et al., *Langmuir* 30, 14931-14943 (2014)
- [7] S.E. de Oliveira et al., *Rev Paul Pediatr.* 33, 230-240 (2012)

- [8] C.E. Probst, P. Zrazhevskiy, V. Bagalkot, X. Gao, *Drug Deliv Rev.* 65, 703-718 (2013)
- [9] R. Wojnarowska-Nowak, *Opto-electron Rev.* 25, 137-147 (2017)
- [10] A.S. Karakoti, R. Shukla, R. Shanker, S. Singh, *Adv Colloid Interface Sci* 215, 28-45 (2015)
- [11] D. Vasudevan, R.R. Gaddam, A. Trinchi, I. Cole, *J Alloy Compd.* 636, 395-404 (2015)
- [12] Y. Wang, L. Chen, *Nanomedicine* 7, 385-402 (2011)
- [13] Szeremeta et al., *Chem Phys*, 456, 93-97 (2014)
- [14] X. Gao, Y Cui, R.M. Levenson, L.W. Chung, S. Nie, *Nat Biotechnol* 22, 969-976 (2004)
- [15] J. Lovrić et al., *J Mol Med (Berl)* 83, 377-385 (2005)
- [16] A. Shiohara, A. Hoshino, K. Hanaki, K. Suzuki, K. Yamamoto, *Microbiol. Immunol.* 48, 669-675 (2004)
- [17] N. Chen et al., *Biomaterials* 33, 1238-1244 (2012)
- [18] X. Bai, S. Xu, J. Liu, L. Wang, *Talanta.* 150 118-124 (2016)
- [19] Q. Yuan, S. Hein, R.D. Misra, *Acta Biomater.* 6, 2732-2739 (2010)
- [20] G. Yordanov, M. Simeonowa, R. Alexandrova, H. Yoshimura, C. Dushkin, *Colloids and Surfaces A: Physicochem. Eng Aspects* 339, 199-205 (2009)
- [21] J.S. Kim et al., *J Colloid Interface Sci* 353, 363-371 (2011)
- [22] S. Huang et al., *Nano Research* 8, 1932-1943 (2015)
- [23] Szeremeta J. et al., *Chem Phys* (2014)

OPTICAL MEASUREMENTS OF COLLOIDAL SEMICONDUCTOR QUANTUM DOTS PHOTOCATALYTIC ACTIVITY

W. Nawrot*, M. Fiedot-Toboła, K. Malecha

Faculty of Microsystem Electronics and Photonics, Wrocław University of Science and Technology,
Janiszewskiego 11/17, 50-372 Wrocław, Poland

*e-mail: witold.nawrot@pwr.edu.pl

Abstract *This work explains what are colloidal quantum dots and what a photocatalytic effect is. Furthermore, applications of such materials and methods of measuring their activity are described.*

Keywords: quantum dot, nanoparticles, photocatalysis

1. INTRODUCTION

Metal oxide semiconductors, such as ZnO and TiO₂, exhibit many interesting features, such as electroluminescence [1], piezoelectricity [2] and photoelectricity [3] [4]. Moreover they are nonstoichiometric and therefore very good materials for gas sensors and biosensors development [5]. Widely studied is also their photocatalytic activity [6] [7]. They are used as antibacterial and antifungal substances. However, those properties are not stable and not fully investigated. Moreover photoluminescence seems to be common side effect. In order to properly examine this subject, a complex laboratory setup needs to be developed. In this work previous, current and future solutions are described, as well as principles on which they rely. Also properties of popular colloidal metal oxides are described.

2. MATERIAL CHARACTERISTICS

2.1 The photocatalytic effect

Most common photocatalytic materials e.g. zinc oxide and titanium dioxide are have very similar properties. They are both wide energy gap metal oxide semiconductors. Typical values are 3.3 eV for ZnO [8] and either 3.26 eV, 3.02 eV or 2.96 eV for TiO₂, depending on its crystal structure [9] and [10]. They correspond with threshold excitation wavelengths of accordingly: 376 nm for zinc oxide and between 380 nm and 419 nm for titanium dioxide, as photon energy can be defined as:

$$E = \frac{hc}{\lambda} \quad (1)$$

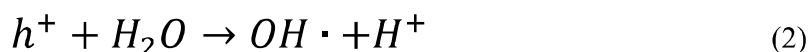
h – Planck constant ($6,63 \cdot 10^{-34}$ J·s)

c – speed of light in vacuum ($3 \cdot 10^8$ m/s)

λ – wavelength [m]

The wide bandgap of zinc oxide and titanium dioxide means that they can be excited by an ultraviolet light. When a photon with enough energy is absorbed, an electron passes from valence band to conduction band, leaving a hole. If no reagents are present, a recombination will occur, i.e. the electron will come back to its original state. Three major types of such phenomenon can be distinguished: Shockley–Read–Hall, Auger or radiative (featuring emission of a photon). However though, these materials most commonly react with surrounding compounds. The key parameter of such reaction is a redox potential – it determines if reduction or oxidation will occur. If this value is above valence band, the electron from a reagent will pass to this band and combine with the hole arose during absorption. If the potential is lower than the conduction band, the excited electron from semiconductor will pass onto reagent and thus reduction will take place.

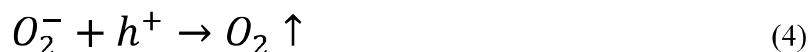
Typically those reactions involve either water molecules or hydroxyl groups. They have a redox potential above valence band, thus the oxidation occurs. This leads to generation of free radicals (OH[•]):



Those radicals are strong oxidisers, which leads to decomposition of many organic substances to water and carbon dioxide. Moreover zinc oxide and titanium dioxide are nonstoichiometric materials, i.e. real metal – oxygen properties are not such as in structural formula. As a result oxygen atoms are easily adsorbed on the surface, leading to formation of a depletion layer:



Some of the holes arose during photon absorption recombines with redundant electrons of those oxygen ions, which results in oxygen emission:



In this process more conductive electrons are present in the material than holes, therefore the recombination time is long, which means that the oxidation potential is high.

2.2 Nanoscale effects

The interest in nanomaterials is constantly increasing due to their unique properties, often significantly different than in bulk materials. Two phenomena can be distinguished as sources of this behaviour: square-cube law and quantum size effect. The first one is a basic mathematical principle, which describes change of surface to volume ratio while scaling. This however has major implications in nanotechnology as bulk phenomena no longer dominates. Particles are very small, i.e. consist of only few molecules. This means that only a limited number of states for electrons is allowed, which consequently influences wave functions of carriers. Therefore a classical physics is no longer accurate and quantum laws are needed. Depending on how many dimensions are nanoscale, three different types of structures can be distinguished: quantum well (1D), quantum wire (2D) and quantum dot (3D). In colloids of semiconductor nanoparticles, such as zinc oxide or titanium dioxide the dielectric stabiliser acts as a potential barrier, making each particle a quantum dot. Therefore these systems are liable to foresaid quantum size effect. The main consequence is a change of bandgap dimension depending on the size of a particle, as shown below [11]:

$$E_{nano} = E_0 + \frac{h^2}{8R^2} \left(\frac{1}{m_e^*} + \frac{1}{m_h^*} \right) - \frac{1,8e^2}{4\pi\epsilon_r\epsilon_0R} \quad (5)$$

E_{nano} – bandgap value in nanoscale [eV]

E_0 – typical bandgap value [eV]

h – Planck constant ($6,63 \cdot 10^{-34}$ J·s)

R – nanoparticle radius [m]

m_e – effective electron mass [MeV/c²]

m_h – effective hole mass [MeV/c²]

e – electron charge ($1,602176620898 \cdot 10^{-19}$ C)

ϵ_r – material dielectric constant [-]

ϵ_0 – vacuum dielectric constant ($8,854187817 \cdot 10^{-12}$ F/m)

Therefore, the smaller the average size of nanoparticle is, the bigger is the bandgap. Consequently the shorter wavelength is needed to excite electrons and to obtain photocatalytic effect. One of the side effects is that the more uniform the size of nanoparticle is, the narrower the spectra of absorbance is.

3. OPTICAL MEASUREMENTS

Typical setups for measuring photocatalytic activity in semiconductor colloids use dyes as an indicator. Under UV light the photocatalytic effect causes decomposition of the pigment, which is quantified by absorbance measurement. The experiment includes two steps. In first the colloid mixed with dye is irradiated under a UV lamp and constantly mixed using a magnetic stirrer for uniform interaction, as show in Fig. 1.

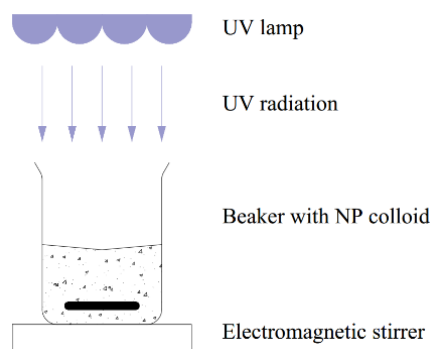


Fig. 1. Laboratory setup for colloid UV irradiation

Then samples are taken in constant intervals (e.g. 30 min) and their absorbance is measured. Exemplary results are show in Fig. 2. The spectra values are decreasing, which represents decomposition of the pigment.

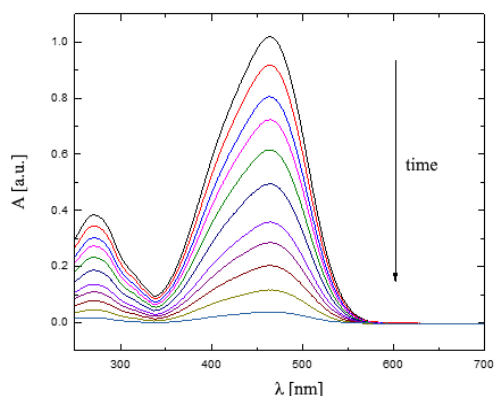


Fig. 2. Change in absorbance of methyl orange dyed TiO_2 NP colloid during UV irradiation (based on [12])

The main issue of this method is discretisation of measurement – interval times are a compromise between resolution and interference in process.

A tailor made laboratory setup was made to provide constant measurement during irradiation. Furthermore it was made as a Lab on Chip solution, which requires less amount of reagents and less energy. Moreover the whole process is accelerated, due to smaller volume. The system was simplified by substituting the spectrophotometric measurement with selective absorbance analysis using colour LED. The spectra of the diode overlaps with chosen dye, such as methyl orange (Fig. 3) or phenolphthalein. A photodiode was used for measuring intensity of passing light. Such setup is cheap, yet sufficient for assessment of photocatalytic activity. The exemplary results are shown in Fig. 4. The pigment is decomposed even without UV irradiation, but reaches a threshold after short time, whereas excitation cases acceleration of the process and provides better results. Furthermore those results show that the whole process takes no more than 15 minutes, compared to several hours in previous setup.

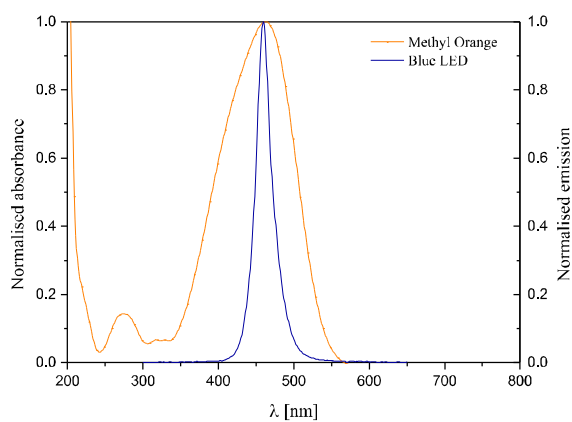


Fig. 3. Methyl orange and blue LED spectra overlap

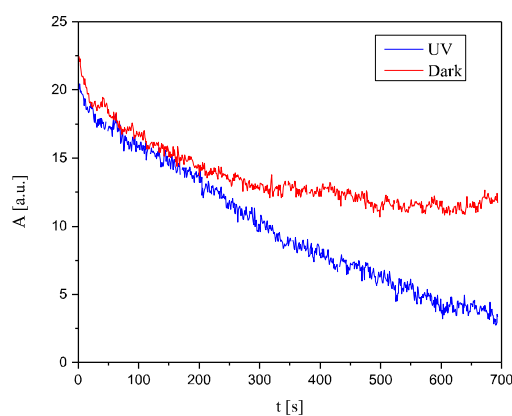


Fig. 4. Change in absorbance with and without UV irradiation

The biggest advantage of developed laboratory setup is the possibility of constant measurement. It enables observation of all the phenomena during process. One of such is photoluminescence. It appears as a rise of solution transmittance during irradiation, above the reference value (i.e. water transmittance) and disappears quickly after (Fig. 5). This phenomenon could not be observed during measurements using spectrophotometer, as in previous setup, because of the sample collection time.

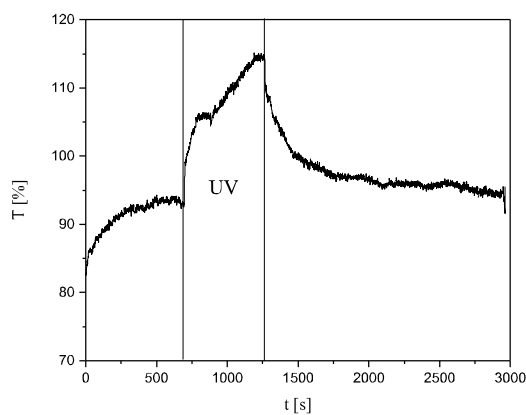


Fig. 5. Photoluminescence during UV irradiation

In order to closely examine the photoluminescence effect in quantum dot colloid a further modifications are needed. Simplified absorbance measurement does not allow spectral analysis. Therefore a spectrophotometric microsystem setup is needed complete description of the process.

Acknowledgement

This work was financed using statutory funds no 0401/0039/17 (Wrocław University of Science and Technology, Faculty of Microsystem Electronics and Photonics).

References

- [1] P. Suchorska-Woźniak, W. Nawrot, O. Rac, M. Fiedot i H. Teterycz, Improving the sensitivity of the ZnO gas sensor to dimethyl sulfide, *Materials Science and Engineering*, 104 (2016)
- [2] J. C. Fan, S. L. Chang i Z. Xie, ZnO-Based Light-Emitting Diodes, *Optoelectronics - Advanced Materials and Devices*, InTech, (2013)
- [3] D. Tamvakos, S. Lepadatu, V. -A. Antohe, A. Tamvakos, P. M. Weaver, L. Piraux, M. G. Cain i D. Pullini, Piezoelectric properties of template-free electrochemically grown ZnO nanorod arrays, *Applied Surface Science*, 356, 1214-1220 (2015)
- [4] Y. Li, X. Liu, X. Chen, D. Wang i Y. He, Photoelectric properties of graphene oxide–ZnO composite nanosheets vertically grown on substrate, *Journal of Alloys and Compounds*, 699, 468-478 (2017)
- [5] H. Wang, X. Tan i T. Yu, Preparation and photoelectric property of TiO₂ nanoparticles with controllable phase junctions, *Applied Surface Science*, 321, 531-537 (2014)
- [6] S. I. Al-Mayman, S. M. Al-Johani, M. M. Mohamed, Y. S. Al-Zeghayer, S. M. Ramay, A. S. Al-Awadi i M. A. Soliman, TiO₂ - ZnO photocatalysts synthesized by sol–gel auto-ignition technique for hydrogen production, *International Journal of Hydrogen Energy*, 42, 5016-5025 (2017)
- [7] M. -Y. Xie, K. -Y. Su, X. -Y. Peng, R. -J. Wu, C. Murthy i W. -C. Chang, Hydrogen production by photocatalytic water-splitting on Pt-doped TiO₂–ZnO under visible light, *Journal of the Taiwan Institute of Chemical Engineers*, 70, 161-167 (2017)
- [8] Z. L. Wang, Zinc oxide nanostructures: growth, properties and applications, *Journal of Physics: Condensed Matter* 25, R829-R858 (2004)
- [9] T. Zhu i S.-P. Gao, The Stability, Electronic Structure, and Optical Property of TiO₂ Polymorphs, *The Journal of Physical Chemistry C* 118, 11385-11396 (2014)
- [10] O. Carp, C. Huisman i A. Reller, Photoinduced reactivity of titanium dioxide, *Progress in solid state chemistry* 32, 33-177 (2004)
- [11] R. Koole, E. Groeneveld, D. Vanmaekelbergh, A. Meijerink i C. de Mello Donegá, Size Effects on Semiconductor Nanoparticles, *Nanoparticles: Workhorses of Nanoscience* (2014)
- [12] D. Oleś, Opracowanie metody syntezy i badanie właściwości fotokatalitycznych nanocząstek dwutlenku tytanu, Politechnika Wrocławska, Wrocław (2013)

ATOMIC FREQUENCY STANDARD

J. Niemczuk^{*}, P. Knapkiewicz^{**}

Faculty of Microsystem Electronics and Photonics, Wrocław University of Science and Technology,
Janiszewskiego 11/17, 50-372 Wrocław, Poland

^{*}e-mail: jakub.niemczuk@student.pwr.edu.pl

^{**}e-mail: pawel.knapkiewicz@pwr.edu.pl

Abstract *We have undertaken the development of a cesium atomic clock which uses the CPT (Coherent Population Trapping) effect for stabilizing synthesized frequency. The main purpose of this project is to build a fully functional frequency standard that will compare to units available on the market, but made entirely out of cheap and widely available components, using simple building techniques.*

Keywords: optoelectronics, 3D FDM printing, spectroscopy, frequency standard

APPLICATION OF DEEP REACTIVE ION ETCHING FOR NANOSTRUCTURISATION OF GAN STRUCTURES

S. Owczarzak*, A. Stafiniak, R. Paszkiewicz

Faculty of Microsystem Electronics and Photonics, Wrocław University of Science and Technology,
Janiszewskiego 11/17, 50-372 Wrocław, Poland

*e-mail: slawomir.owczarzak@pwr.edu.pl

Abstract *The fabrication of the piezotronic devices requires fabrication of deeply etched structures that could be obtained using deep reactive ion etching technique. Two different sets of RIE process parameters such as pressure, temperature, gas flow and RF power were studied for fabrication of trenches with various depth. The inclination angle of trenches sidewall, their etched surface roughness profile and the depth were investigated in detail using atomic force microscopy and scanning electron microscopy. The article will present the results of the study of AlGaIn/GaN HEMT heterostructures deep reactive ion etching process performed using chlorine based plasma and dielectric hard-masks.*

Keywords: AlGaIn/GaN, DRIE, piezotronic devices, deep trenches, side walls inclination

1. INTRODUCTION

Materials of AIIIIN group except good electrical parameters such as breakdown voltage, electron velocity, possibility of controlling the energy gap from 0.72 eV to 6.2 eV. These materials also have promising piezoelectric parameters enabling their application for fabrication of piezotronic devices. Majority of piezotronic devices required etched depth trenches with perpendicular side walls. Due to that reactive ion etching (RIE) process must be performed with high etch rate. The effect of Cl₂ and Ar gases flow rate on etching rate was studied in literature [1] using inductive coupled plasma (ICP) technique. The highest etch rate that was obtained using capacity coupled plasma (CCP) was 75 nm/min [2]. In the article the results of the research of CCP RIE process for deep etching of AlGaIn/GaN HEMT heterostructures will be presented and discussed.

2. EXPERIMENT DETAILS

The first step of experiment was selection of optimal parameters of RIE process using Taguchi method for experiment planning [3]. Nine sets of RIE process parameters were chosen: pressure between 15 and 35 mTorr, temperature between -13 and 27 °C, hard-mask thickness between 70 nm and 350 nm as well as different mixtures of reactive plasma gases Cl₂/BCl₃/Ar with constant total gas flow of 15 sccm (the Ar flow was kept 5 sccm) and constant RF power of 170 W. SiO₂ hard-masks were deposited using plasma enhanced chemical vapour deposition (PECVD) technology on heterostructures. Before RIE process, all samples were cleaned using HCl. The influence of temperature, pressure, reactive gas mixture on etch rate were studied and are presented in Figure 1. and Figure 2. The results of first step of experiment were delimitation of RIE process parameters such as pressure, temperature and Cl₂/BCl₃/Ar ratio. That optimal RIE process allow to obtain 56 nm/min

etch rate and maximal inclination of side walls as high as 39° and the selectivity value [semiconductor: hard-mask] equal to 4.

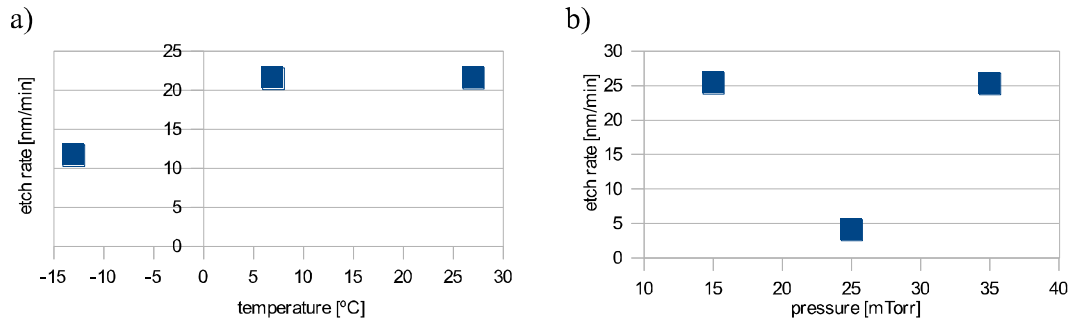


Fig. 1. Influence of temperature a) and pressure b) on etch rate of AlGaIn/GaN HEMT structures in RIE process

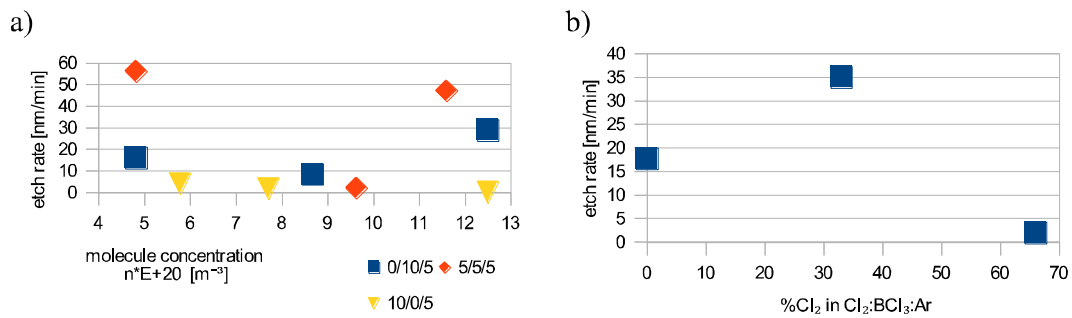


Fig. 2. Influence of concentration a) and percentage of Cl₂ in Cl₂/BCl₃/Ar b) on etch rate of AlGaIn/GaN HEMT structures in RIE process

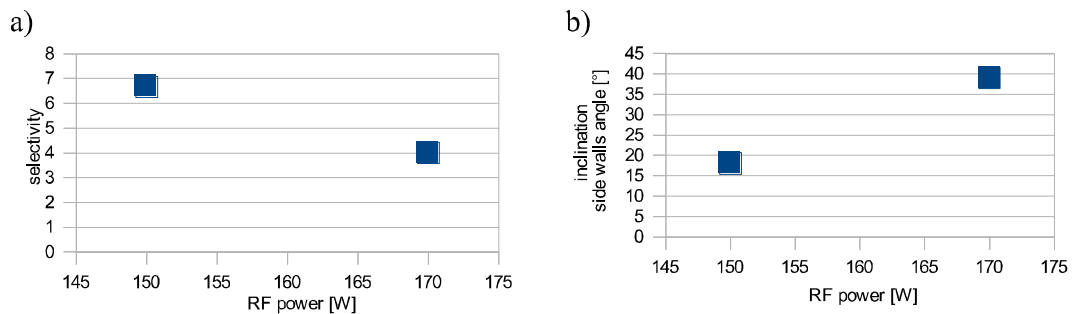


Fig. 3. Influence of RF power RIE on a) selectivity and b) sidewall inclination of AlGaIn/GaN HEMT structures etched in RIE

Knowing temperature and pressure in chamber, for each mixture of reactive gases enabled the calculation of molecules concentration. This led to the conclusion that independently from reactive gases mixtures, for molecules concentration from $8 \cdot 10^{20} \text{ m}^{-3}$ to $10 \cdot 10^{20} \text{ m}^{-3}$, the etch rate is the lowest. In the next step the influence of decreasing of RF power on surface morphology was studied. The obtained results illustrating the influence of RF power on selectivity of heterostructures etching to mask, inclination of side walls as well as etch rate are presented in Figure 3. and Figure 4. Decreasing of RF power from 170 W to 150 W caused the drop of etch rate to 16 nm/min, significant reducing the inclination of side walls and increasing of etch selectivity from 4 to 6.6.

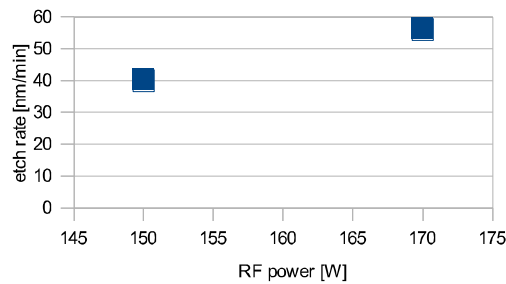


Fig. 4. Influence of RF power RIE on etch rate of AlGaIn/GaN HEMT structures

3. THE FABRICATION OF DEEP TRENCHES

For deep etched structure fabrication two different mixture of reactive gases and RF power, were selected, which are presented in Table 1. The chosen gas flow and RF power during execution of the recipe no. 2 were based on the literature [4].

Table 1. Two sets of etch DRIE process parameters

No. recipe	Temperature [°C]	Pressure [mTorr]	RF power [W]	Cl ₂ [sccm]	BCl ₃ [sccm]	Ar [sccm]
1.	7	15	170	5	5	5
2.	7	15	250	16	4	5

Impact of trench depth of etched structures on etch rate and inclination of side walls are presented in Figure 5. Deep reactive ion etching (DRIE) of samples were processed for 5 min, 12 min and 18 min. It should be noted that together with depth increasing of the etched structures, the etch rate was decreased, because in deep structures efficiency of reaction products removal is reduced therefore etch rate is decreases. The most inclined side walls were obtained using process number 2. Side walls of structures etched to the depth of 625 nm were inclined at an angle 62°. SEM images of obtained structures/trenches are presented in Figure 6. Width of trenches varies from 2 to 16 μm.

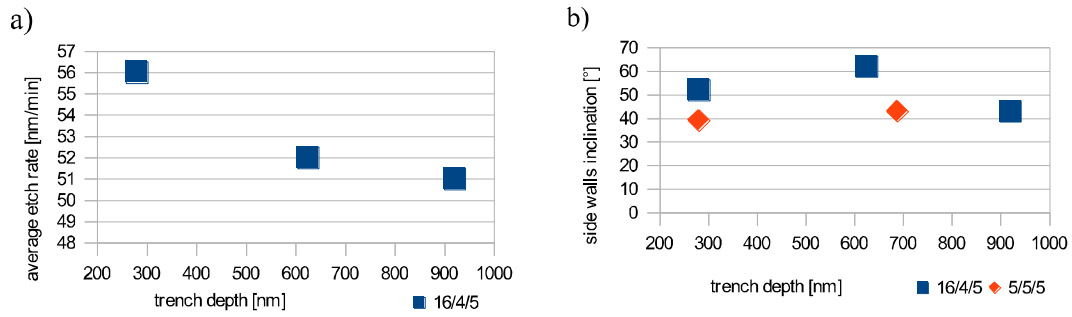


Fig. 5. Influence of etch time on depth a) and influence of trench depth on side walls inclination b) Influence of trench depth on etch rate a) and side walls inclination b)

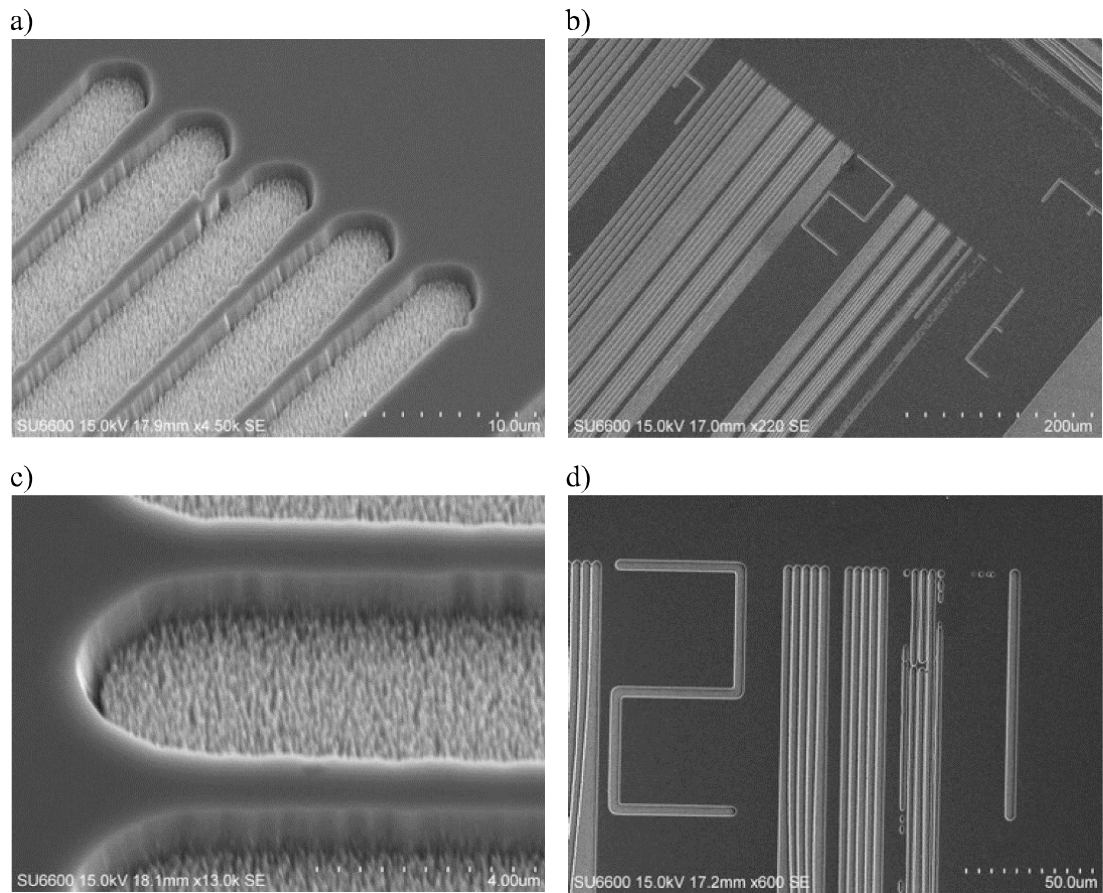


Fig. 6. SEM images of structures etched during 18 min using recipe no. 1 a) b) and recipe no. 2 c) d)

4. CONCLUSIONS

It was established that for fabrication of structures containing deep trenches the process number 2 was better than process number 1, because of the increased chlorine flow and total flow of reactive gases as well as increased ions energy in plasma. In the range of RF power from 150 W to 250 W, the selected optimal temperature and pressure of RIE process were 7 °C and 15 mTorr. To etch the structures of 1 µm depth the 20 min duration of RIE process was needed. Because standard AlGaIn/GaN HEMT heterostructures have about 2.5 µm thickness, 1 hour duration of RIE process will be necessary to etched the trench to the sapphire substrate. To stabilize the etch rate and to increase the inclination of side walls the increasing of reactive gases flow is mandatory. Low etch rate is a serious problem because in each of studied RIE processes with out ICP the etch rate did not exceed 60 nm/min.

Acknowledgement

This work was co-financed by the European Union within the European Regional Development Fund, through a grant from the Innovative Economy (POIG.01.01.02-00-008/08-05), by the National Centre for Research and Development through the Applied Research Program Grant No. 178782, the program LIDER No. 027/533/L-5/13/NCBR/2014, the National Science Centre under Grant No. DEC-2015/19/B/ST7/02494, by Wroclaw University of Science and Technology statutory grants and by the Slovak-Polish International Cooperation Program

References

- [1] Chih-Chiang Kao, H.W. Huang, J.Y. Tsai, C.C. Yu, C.F. Lin, H.C. Kuo* , S.C. Wang, Study of dry etching for GaN and InGaIn-based laser structure using inductively coupled plasma reactive ion etching, *Materials Science and Engineering B107* (2004) 283–288
- [2] Mike DeVre, Russ Westerman, Graham Muir, Laurent Bellon, *Advances in GaN Dry Etching Process Capabilities*, Compound Semi & Microtechnology, Unaxis Wafer Processing
- [3] S. Owczarzak, A. P. Stafiniak, R. Paszkiewicz, Application of deep RIE technology for piezotronic device fabrication, *5th International Conference on Advances in Electronic and Photonic Technologies: proceedings of ADEPT, Podbanské, High Tatras, Slovakia, June 19-22, 2017 / [eds. I. Lettrichová, L'. Šušlik, J. Kováč, jr.]*. [Žilina: University of Žilina, 2017]. s. 80-83.
- [4] R. J. Shul,¹ M. A. Miller,¹ M. H. Crawford,¹ J. Stevens,¹ A. A. Allerman,¹ K. H. A. Bogart,¹ M. Banas,¹ K. C. Cross,¹ J. Wright,² and S. J. Pearton², Anisotropic, Smooth High-Density Plasma Etching of GaN/AlGaIn for Etch Facet Laser Applications, 214th ECS Meeting The Electrochemical Society

ELABORATION OF AR-SERIES RESISTS BASED PHOTOLITHOGRAPHY FOR MICROELECTRICAL DEVICES FABRICATION

A. Piejko¹, J. Prazmowska^{2,*}, R. Paszkiewicz²

¹ Faculty of Fundamental Problems of Technology,
Wybrzeże Wyspiańskiego 27, 50-370 Wrocław, Poland

² Faculty of Microsystem Electronics and Photonics,
Wrocław University of Science and Technology,
Janiszewskiego 11/17, 50-372 Wrocław, Poland

*e-mail: joanna.prazmowska@pwr.edu.pl

Abstract *Photolithography is a process in which a pattern is transferred into a surface covered by photoresist. Depending on the type of technique, additive or subtractive, e.g. electrical connection or etching is possible.*

This process contains surface preparation, spinning of photoresists on the surface, exposition through the mask and development. The aim of the work was elaboration of AR-series resists based photolithography process for the purpose of microelectronic devices fabrication. The one-layer (standard) as well as lift-off lithography on Si and AlGaIn/GaN heterostructures were studied. The preliminary tasks embraced estimation of thicknesses of top and bottom layers for various spin-coating velocities. Further dependence of undercut depth on time of development was estimated. Based on the results the applicability of AR-series resists for microelectronic devices fabrication was discussed.

Keywords: lift-off, microelectronic devices, photolithography

1. INTRODUCTION

Photolithography is a process in which a pattern is transferred into a surface. This process contains surface preparation, spinning of photoresists on the surface, exposition through the mask with chrome patterns and development. After that, further microelectronic processes could be conducted. The lift-off is a type of photolithography technique, where after resists development another layer is deposited (eg. metallization) on top of the sample to form a pattern. Redundant resist and metallization are removed in stripping process. The photolithography is complicated, multi-stage process thus variety of parameters influence the results. The most important of them are thickness of resists layers, time of exposure, time of development and environmental conditions as e.g. temperature.

Resist profile strongly depends on exposure dose and post-exposure baking parameters. The post-exposure baking process assures drying of the photoresist after spin coat by removing excess solvent. The aim of reducing the solvent content is stabilization of the resist film parameters.

If the time of exposure is too long the photoresist image will be eroded along the edges, what leads to decrease in size and a loss of sharpness or corners. In the other side, if time of exposure is too short, image will be underexposed. If image is underexposed, the

pattern may not be transferred at all to the surface. Overexposure or overdevelopment will deteriorate the profile of the unexposed surface.

It is difficult to obtain a uniform resist coat across a surface with developed topography, what complicates exposure and development as the resist has different thicknesses on the surface. In the work the homogeneity of resist thickness was also studied and discussed.

2. EXPERIMENTAL DETAILS

The AR-P 3120 (herein as AR-P) positive photoresist and AR-BR 5480 (herein as AR-BR) bottom resist (AllResists) were tested to optimize the photolithography parameters for microelectronic devices fabrication. Series of Si/SiO₂ test wafers and AlGa_N/Ga_N/Al₂O₃ (SiO₂ covered - only for mesas formation step) samples were used. Investigations embraced application of AR-P for standard lithography (mesa formation) while AR-BR/AR-P were dedicated for lift-off technique investigation. There were two different aims of conditions optimization for lift-off test, a) high resolution and b) medium resolution. In the first one spin speed and time of baking of AR-BR and AR-P photoresist were 6000 rpm, 5 min at 150 °C and 3000 rpm, 1 min at 100 °C, respectively. In second one case, AR-P resist spinning parameters were the same as in first case and for AR-BR were 4000 rpm, 5 min at 150 °C. After spinning, the samples surface was exposed through the test chromium mask. Next, samples were developed in AR 300-47:DI (1:1) solution, which removes unexposed part of photoresist layer.

One of the crucial requirement for resist/sample system is appropriate adhesion. Silicon oxide as well as AlGa_N/Ga_N needed the AR 300-80 adhesion promoter support. The promoter insured covalent binding of samples surface and resist, improving the adhesion strength.

In the work the thicknesses of resists for various spin speeds were evaluated using scanning electron microscope (SEM). Additionally thickness uniformity of the AR-BR on sample surface as well as resistance of AR-P 3120 photoresist to BHF (in a purpose of standard lithography) were discussed. Also dependence of undercut depth on time of development in lift-off technique was estimated and studied.

During the process of mesas formation the BHF, which is a mixture of ammonium fluoride (NH₄F) and hydrofluoric acid (HF), was used for etching of SiO₂ thus resistance of resist to this solution is an essential property. The Si test wafers with exposed AR-P layer were studied. A half of the sample surface was masked using blue-tape. Then BHF bath for 5 min at 22 °C, DI rinsing and N₂ drying were carried out.

In the work test line-space masks as well as microelectronic devices structures chromium masks were used.

3. RESULTS AND DISCUSSION

3.1 Homogeneity of AR-BR 5480 resist thickness

The homogeneity of AR-BR resist thickness was evaluated by measuring the thickness in various places on the sample (spin speed was equal to 4000 rpm). The AR-P spin speed was 3000 rpm and time of development 60 s. Example SEM images are shown in Fig. 1.

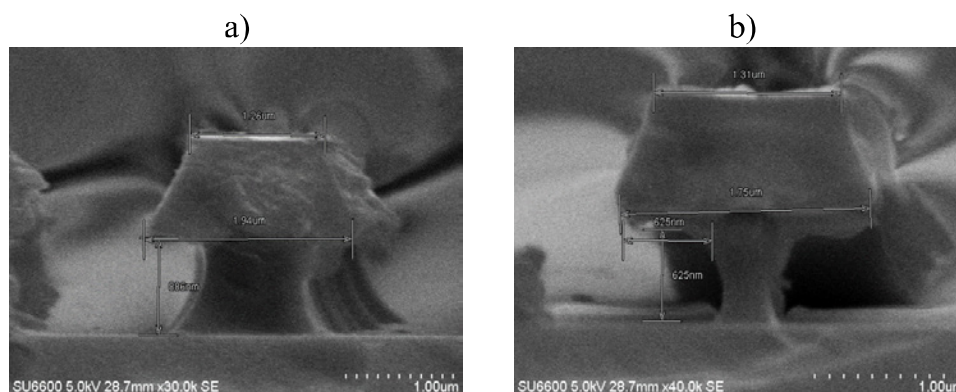


Fig. 1. SEM images of various undercut depth (the same spin speed of AR-BR)

Thickness variation among the sample was in the range from 500 to 600 nm. It led to significant non-uniformity in undercut depth (Fig. 2). The problem was overcome by changing the parameters of first step of resist spinning. The maximum obtained variation in layer thickness was of 50 nm.

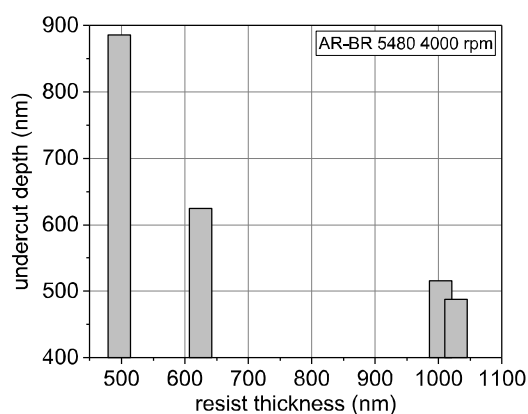


Fig. 2. Undercut depth dependence on AR-BR layer thickness

3.2 Dependences of layer thickness on spin speed

The AR-P and AR-BR resists were spin-coated on substrate surfaces with different spin speeds (AR-BR 2000-7000 rpm while for AR-P from 2000 to 5000 rpm). The soft-baking parameters were as described earlier. Thicknesses of layers depending on spinning speed are presented in Fig. 3. a) and b). Dependence of layer thickness on spin speed was linear for small values of spin speeds and saturated for larger values, as expected. Obtained results permitted for selection of spin speeds appropriate in further studies for medium and high resolution tests.

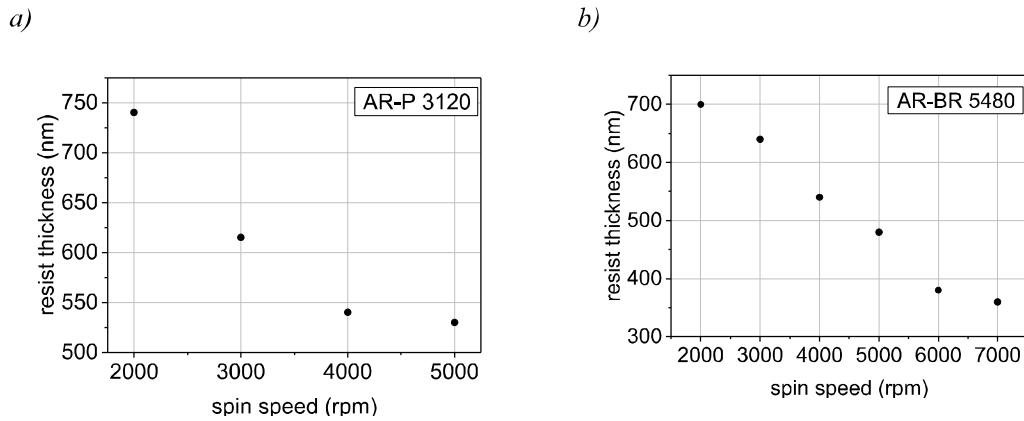


Fig. 3. Thicknesses of a) AR-P 3120 and b) AR-BR 5480 resists for different spin speeds

3.3 Resistance of AR-P 3120 photoresist to BHF

The BHF bath duration exceeded strongly the etching time used during processes. Images of samples surface before and after BHF bath are shown in Fig. 4.

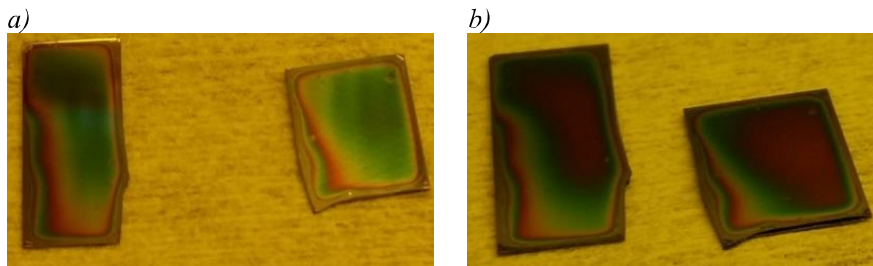


Fig. 4. Images of surface of resists before a) and after b) BHF bath

The BHF treatment did not affect the morphology of the samples surfaces. Also SEM imaging did not reveal any changes in geometrical parameters of samples. It could be also assumed that chemical properties of the resist layer remained unchanged because of further, successful stripping of the photoresist.

3.4 Dependences of undercut depth on time of development

Test were carried out for AR-P/AR-BR bilayer exposed through 6s. Spin speed for top layer was 3000 rpm in each case. Spin speed for bottom layer were from 4000 to 7000 rpm. Time of development varied from 45 to 60 s. The dependence of undercut depth on time of development is presented in Fig. 5.

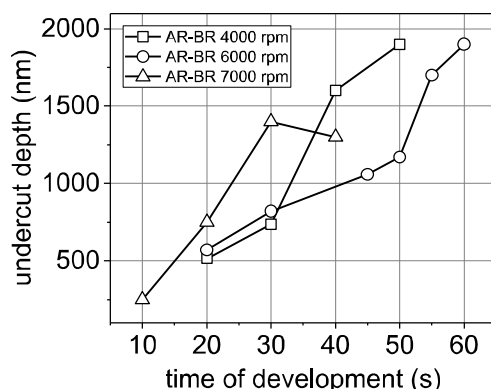


Fig. 5. Dependence of undercut depth on time of development

It could be observed that thicker layers of AR-BR (4000 rpm) exhibited larger undercut depth than thinner layers for the same time of development. Observed phenomenon could be explained by low efficiency of reaction product exchange in thinner layers.

Obtained results gave an important information for the fabrication of microelectronic devices. Standard lithography and ohmic contact fabrication were successfully conducted using AR-P and AR-BR resists.

4. SUMMARY

The AR-series resists were studied for standard and lift-off application. Layer thickness decreased nearly linearly with increasing spin speed (within studied range of spin speed). Top layer may be applied as single layer for standard lithography cause of resistance in BHF. In some cases adhesion promoter was needed to improve adhesion strength. Double layer system was studied and successfully applied for ohmic contacts patterns formation. In the future application of double layer system for gates pattern fabrication could be studied with decrease of AR-BR 5480 layer thickness.

Acknowledgement

This work was co-financed by the European Union within the European Regional Development Fund, through a grant from the Innovative Economy (POIG.01.01.02-00-008/08-05), by the National Centre for Research and Development through the Applied Research Program Grant No. 178782, the program LIDER No. 027/533/L-5/13/NCBR/2014, the National Science Centre under Grant No. DEC-2015/19/B/ST7/02494, by Wrocław University of Science and Technology statutory grants and by the Slovak-Polish International Cooperation Program.

References

- [1] Wayne M. Moreau, *Semiconductor Lithography: Principles, practices, and materials*.
- [2] Stephen A. Campbell, *Fabrication Engineering at the Micro- and Nanoscale*.

3D PRINTED MEMBRANE-BASED GAS MICROFLOW REGULATOR

A. Podwin

Faculty of Microsystem Electronics and Photonics, Wrocław University of Science and Technology,
Janiszewskiego 11/17, 50-372 Wrocław, Poland
e-mail: agnieszka.podwin@pwr.edu.pl

Abstract *This paper reports fabrication and characterization of a miniature 3D printed membrane-based gas microflow regulator. In the device, a polydimethylsiloxane (PDMS) diaphragm was applied to act as a diffusion barrier and adjust gas flow to the desired rate. Repeatable flow values in the function of pressure for various membrane thicknesses and gas types were obtained. The use of 3D printing technique enabled for fabrication simplicity, so that the solution may be easily adapted for a variety of microdevices applied in the field of life sciences.*

Keywords: 3D printing, PDMS membrane, gas microflow, gas regulator

1. INTRODUCTION

At recent times, a dynamic development of lab-on-a-chip platforms intended for versatile bio-based applications has been observed. In such microfluidic systems, considering mainly cell culturing branch, flow regulation constitutes especially important issue. In order to imitate cells *in vivo* environment, a constant and well-controlled medium flow in the lab-on-a-chip device is required. For this reason, an internal structure of the chip is often designed as self-contained system, involving specific valves, separation microchannels or polymer (usually PDMS) diffusion barriers [1]. Nevertheless, such solutions are technologically complex and require a new chip design for each modified experimental demand. On the other hand, commercially available micropumps for medium supply and/or refreshment are basically adjusted to the ranges of ml/min flow, which may seem too intensive for cell culturing applications. Concerning the advantages and weaknesses of the current solutions, a miniature and portable gas flow regulator based on PDMS membrane has been proposed. The device was fabricated utilizing 3D printing technique that due to rapid prototyping, fabrication simplicity and low costs is inevitably increasing in popularity in the bio-scientific fields recently [2-3]. The regulator was successfully applied for cell culturing of microorganisms (euglenas), by the controlled release of 100% carbon dioxide into the chip.

2. EXPERIMENTAL

Basic parts of the regulator (Fig. 1) were fabricated utilizing inkjet 3D printing technique (Projet 3510 printer using Visijet M3 Crystal and Visijet S300 materials, 3D Systems, USA). The device comprises two main elements – inlet and outlet. Inlet part is connected with gas pneumatic line. In the outlet, gas permeable PDMS membrane (Φ 12 mm) and additional functional elements, like o-ring sealing (Φ_{outer} 13 mm, Φ_{inner} 9 mm) and a sieve (Φ 14 mm, via holes in the sieve – Φ 1 mm) are placed. The surface of the sieve is structurized to protect the membrane from break while pressure operation. The membrane

is attached to the sieve by the pressing ring (Φ_{outer} 16 mm, Φ_{inner} 6 mm). Standard connectors may be applied to the inlet and outlet ports. In this solution, a microfluidic connector at the outlet was 3D printed to fit the tube of 1/16'' diameter.

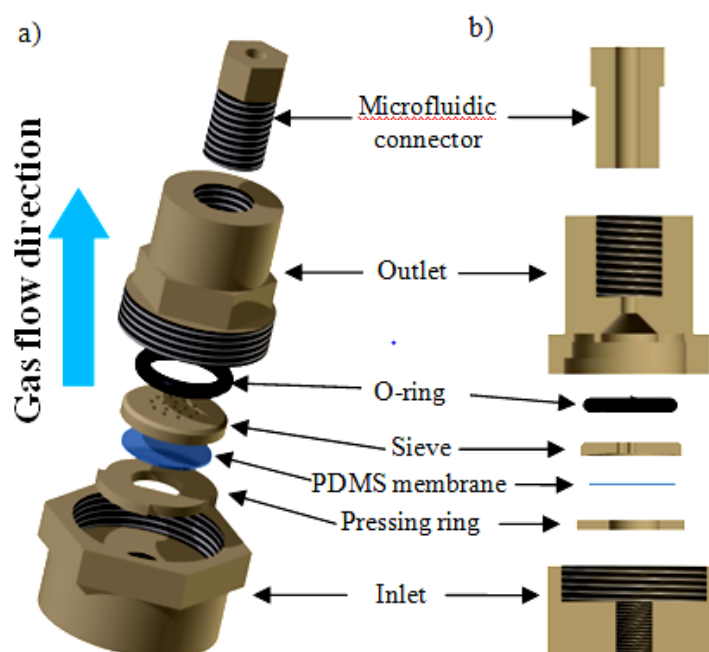


Fig. 1. 3D printed membrane-based gas microflow regulator: a) exploded schematic view, b) cross-section view

The membrane is fabricated utilizing molding technique. PDMS prepolymer (Sylgard 184, Dow Corning, USA) mixed with curing agent at the ratio of 10:1 (w/w) and degassed, is casted onto master mold with desired depth. The polymerization is conducted by heating the mold for 1 h in 70 °C in a furnace.

The structure of the regulator allows for the use of membranes with thicknesses in the range of 200 – 400 μm . The application of PDMS membrane enables for delivery of various gases, like N_2 , CO_2 , CH_4 , C_2H_6 [4]. The overall weight of the device is 10.5 gram only. Fabrication time of 10 regulators is circa 6 h.

3. RESULTS AND DISCUSSION

Measurements of the flow rate, concerning increase and decrease in pressure operation (Fig. 2a), were conducted for three types of gases: air, N_2 , CO_2 (Fig. 2b), and three thicknesses of the PDMS membrane (200, 300 and 400 μm , Fig. 3). The flow was determined using bubble detection method. The image of the bubble size and its number per unit time in the baker with water was acquired by CCD camera, and then processed by the dedicated software to indicate the flow value. Maximum applied pressure during measurements was 1 bar. Statistical analysis proved that flow depends parabolically on applied pressure and changes linearly in reference to the membrane thickness. Differences in flow rate were also observed regarding gas type, due to some diversities of gas molecules size.

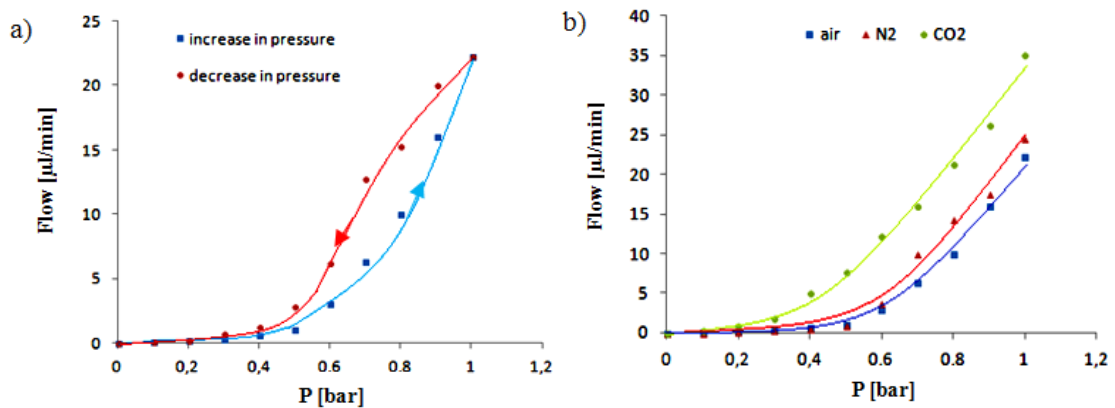


Fig. 2. Flow characteristics of the 3D printed membrane-based gas microflow regulator with 400 μm thick PDMS membrane: a) air flow – visible pneumatic hysteresis, b) flow for the selected gases

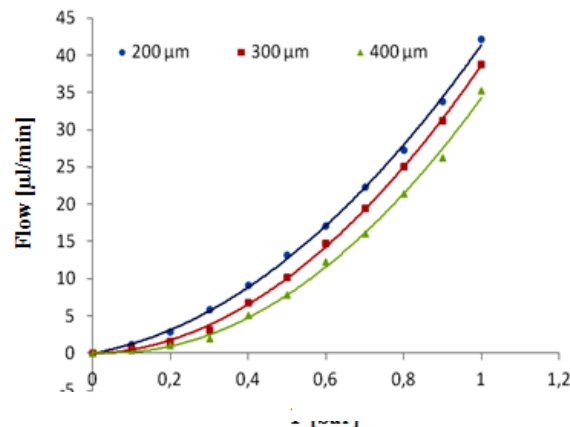


Fig. 3. Carbon dioxide flow characteristics with regard to PDMS membrane thickness

The regulator was successfully applied as a medium supplier to the lab-on-a-chip platform intended for cell culturing of *Euglena gracilis*. Microorganisms performed photosynthesis on-chip by stimulation with 100% CO₂ (flow rate: 0.3 μl/min) and halogen lamp illumination (40 W, 600 lm) for above 10 days (Fig. 4).

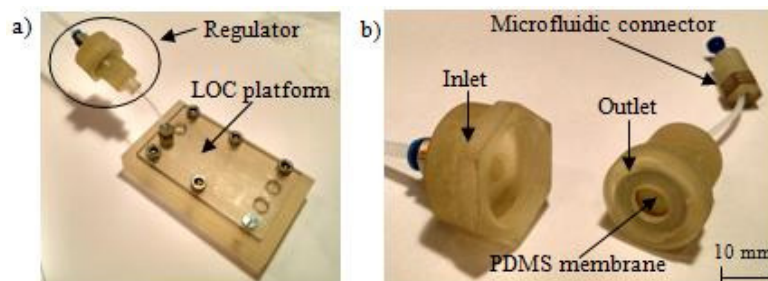


Fig. 4. 3D printed membrane-based gas microflow regulator: a) device integrated with microfluidic platform, b) disassembled regulator view

4. CONCLUSION

In the paper, a novel 3D printed membrane-based gas microflow regulator has been presented. The device allowed for a precise and repeatable dosage of gas medium to the lab-on-a-chip platform for cell culturing. As a result, a long-term culture of *Euglena gracilis* was achieved that confirmed the regulator suitability in life sciences branch.

Acknowledgments

The works were financed by NCN SONATA BIS project no 2013/10/E/518/0342 and Wrocław University of Science and Technology Young Scientists Statutory Grant no 0402/0052/17.

References

- [1] M. Boyd-Moss, S. Baratchi, M. Di Venere, K. Khoshmanesh, *Lab Chip*, 17, 3177-3192 (2016).
- [2] R. Walczak, K. Adamski, D. Lizanets, *J. Micromech. Microeng.*, 27, <https://doi.org/10.1088/1361-6439/aa6152>,(2017).
- [3] K. Adamski, W. Kubicki, R. Walczak, *Procedia Eng.*, 68, 1454-1457 (2016).
- [4] T. C. Merkel, V. I. Bondar, K. Nagai, B. D. Freeman, I. Pinnau, *J. Polym. Sci. Part B*, 38, 415-434 (2000).

INFLUENCE OF BOUNDARY CONDITIONS ON RESULTS OF NUMERICAL ANALYSIS OF PHOTONIC DEVICES

D. Przybylski*, S. Patela

Faculty of Microsystem Electronics and Photonics, Wrocław University of Science and Technology,
Janiszewskiego 11/17, 50-372 Wrocław, Poland

*e-mail: Dariusz.Przybylski@pwr.edu.pl

Abstract *This paper presents different types of numerical boundary conditions used in FDTD calculations. Lumerical software is used to present practical examples of modeling and to show how the selection of the boundary conditions influences results of simulations. The boundary conditions considered here represent a set of assumptions at the edges of the area of numerical analysis. In this paper the following boundary conditions are considered: Bloch, periodic, metal, perfectly matched layer (PML) and symmetric/anti-symmetric. As an exemplary structure, a gallium arsenide solar cell was used. The cell efficiency is improved by an antireflection layer made of 2D photonic crystal. Modelling of such a structure requires proper selection of boundary conditions. Otherwise, results will be time-consuming or erroneous. We used different boundary conditions for calculation of reflectance and transmittance of the exemplary structure. We show how boundary conditions influence results of the numerical analysis.*

Keywords: numerical analysis, photonic crystal, antireflection coatings, boundary conditions

1. INTRODUCTION

One of the stages of building the numerical model of a photonic structure is setting up the numerical boundary conditions (BCs). They are the equations that specify the behavior of the electromagnetic field at the boundaries of calculation area [1]. That area of simulation is usually smaller than the whole device, so we have to pass to the algorithm information about the whole structure, including information about periodicity and symmetry. Correct selection and setting up of the boundary conditions is necessary to build a reliable numerical model.

2. BOUNDARY CONDITIONS

In this paper, the study of the influence of boundary conditions on the result of numerical analysis was executed on a simple model of a solar cell. We used the Lumerical FDTD software for calculations. Lumerical is a commercial-grade simulator based on the finite-difference-time-domain (FDTD) algorithm [2]. The modeled solar cell is made of gallium arsenide (GaAs) of 2 μm thickness. The structure was illuminated by solar spectrum AM1.5, from 300 nm to 1200 nm. The reflection from the top of the solar cell was calculated. The calculations have been done for a set of different boundary conditions. The boundary conditions which we used in our numerical analysis included a perfectly matched layer (PML), metal BC, Bloch BC, periodic BC and symmetric/anti-symmetric BC.

2.1 Perfectly matched layer and metal boundary conditions

Definition of the PML (perfectly matched layer) boundary conditions: PML boundaries absorb electromagnetic waves incident upon them. They model open or reflectionless boundaries [3]. Metal BCs are used to specify boundaries that behave as a perfect electric conductor. The metal boundaries are perfectly reflecting, allowing no energy to escape the simulation volume [3]. It should be stressed out, that these boundary conditions specify how the algorithm process electromagnetic fields at the edges of the modeling area, they do not represent an actual reflection of light from surfaces of the structure.

To check the influence of selection of the BCs we created a model of solar cell without any antireflection coatings on the top. The reflections have been calculated for PML and metal BCs set up as shown in the Fig. 1.

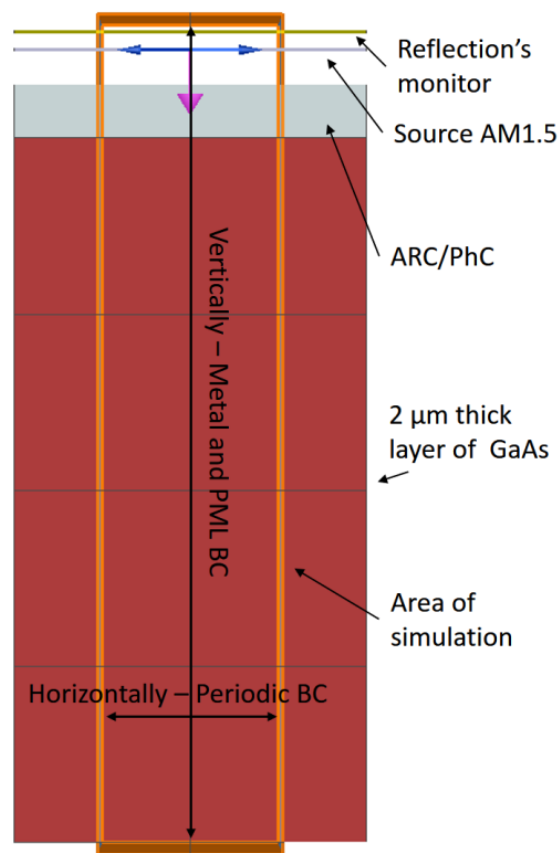


Fig. 1. Configuration of modeling structure and setting up the BCs

In figure 2. you can see the reflection of the light from the top surface of the solar cell for different BCs used in calculations.

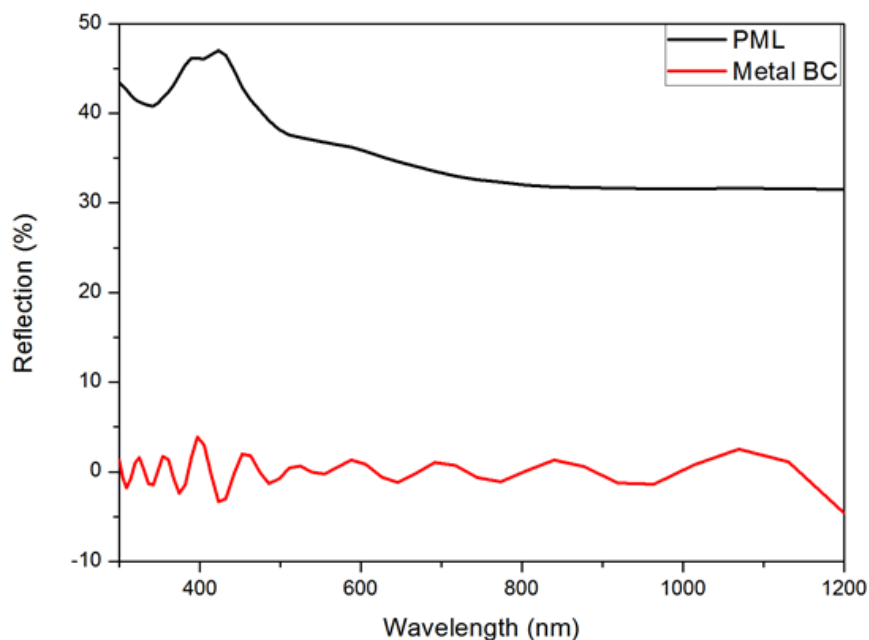


Fig. 2. Comparison the PML and metal boundary conditions setting up vertically

In figure 2. you can see differences between using PML and metal BCs. Correct results are for PML BC because for metal BC the whole modeled structure is treated as an optical cavity. Our modeling results were compared with the measurement data from [4]—reflection from the gallium arsenide layer. The comparison confirmed that the PML is the correct BC for the analyzed solar cell structure. In more advanced structures, for example, with photonic crystal deposited on the top of the structure, the comparing with data from the article or measurements was not possible, due to the differences in structure details.

2.2 Periodic and Bloch BCs

The definition of the periodic BCs: periodic BC should be used when both the structure and electromagnetic field is periodic. Periodic boundary conditions can be used to simulate a structure with a repeatable pattern in one direction but not necessarily other directions [3]. Bloch BC should be used when the structures and the electromagnetic fields are periodic, but the angle-dependant phase shift is present [3]. Either of the two BCs can be applied for the numerical analysis of the similar photonic structures. The periodic and Bloch BCs can be used in simulations of structures with a grating, photonic crystal, or antireflection coating. However, Bloch BC is used when the source is working at an angle relative to the structure. As an example of the influence of selection of these BCs, the model of a solar cell with photonic crystal (PhC) deposited on the top was built. The parameters of the PhC were described elsewhere [5] and the material of PhC was poly(methyl methacrylate) (PMMA). In the figure 3. we compare the periodic and Bloch BCs used in the model of the solar cell. The sides of the structure were controlled by the PML BCs. The light was propagated perpendicularly to surface.

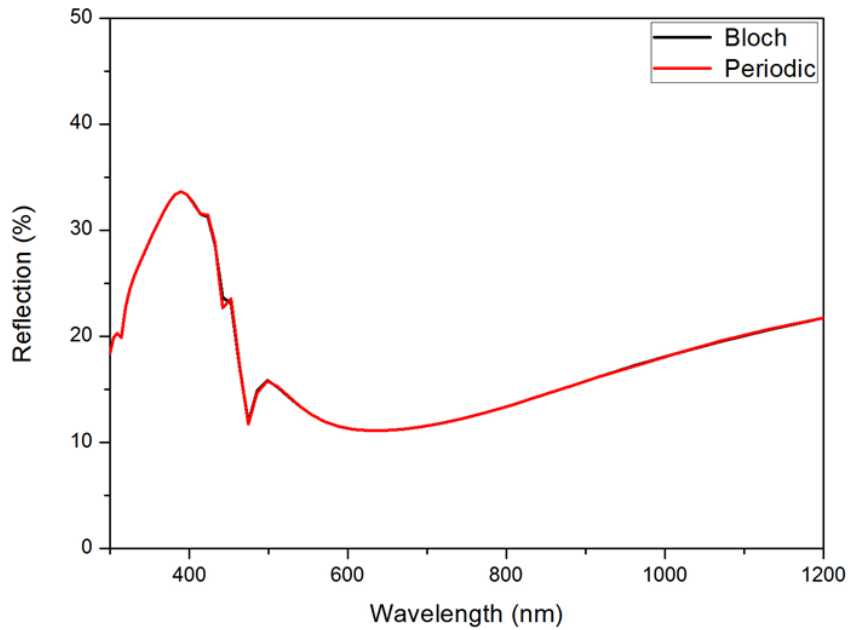


Fig. 3. Comparing the periodic and Bloch BCs when the light is propagated perpendicularly to surface. No visible difference can be seen.

There is no visible difference between results obtained for Bloch and periodic BCs. However, when the angle of incidence is changed from 0° to 10° results are different, with periodic BCs producing unrealistic absorption bands in the reflection spectrum, as shown in Fig. 4.

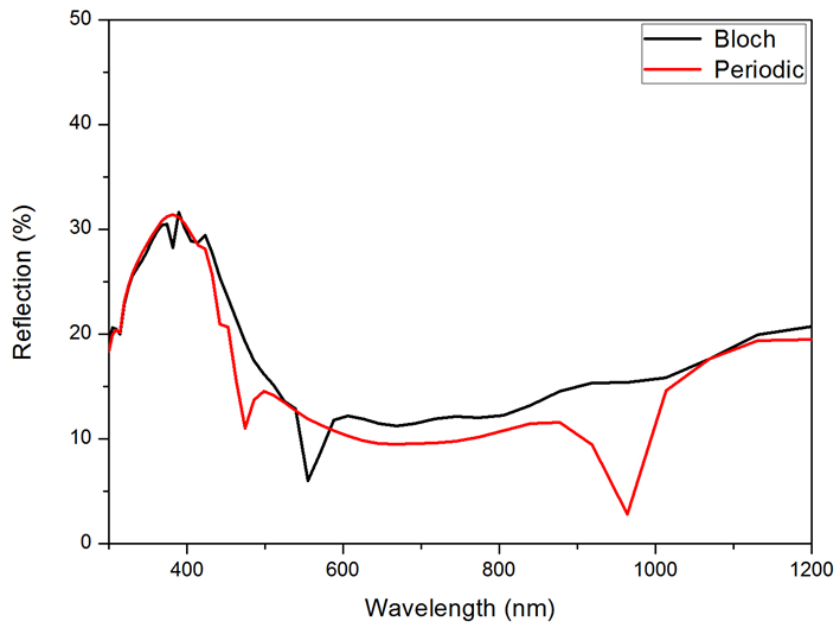


Fig. 4. Comparing the periodic and Bloch BCs when the light is propagated at an angle of 10°

2.3 Symmetric/anti-symmetric BCs

Definition [3]: symmetric/anti-symmetric boundary conditions are used when the user is interested in a problem that exhibits one or more planes of symmetry; both the structure and source must be symmetric. The symmetric BC works as a mirror for the electric field and anti-mirror for the magnetic field. The anti-symmetric BC works as a mirror for the magnetic field and anti-mirror for the electric field. These BCs can only be used if the structure and fields are both symmetric and periodic.

Some prior information about the distribution of electromagnetic field within the analyzed structure is required to apply these BCs. Results of using the symmetric or antisymmetric BCs is shown using the solar cell structure described previously. PMLs were used as vertically BC, limiting the modeling area on the sides. The comparison of the reflection of light from the structure, obtained for different BCs is shown in figure 5. As expected, symmetric and antisymmetric BCs produce unrealistic results, as the structure does not introduce and explicit symmetries.

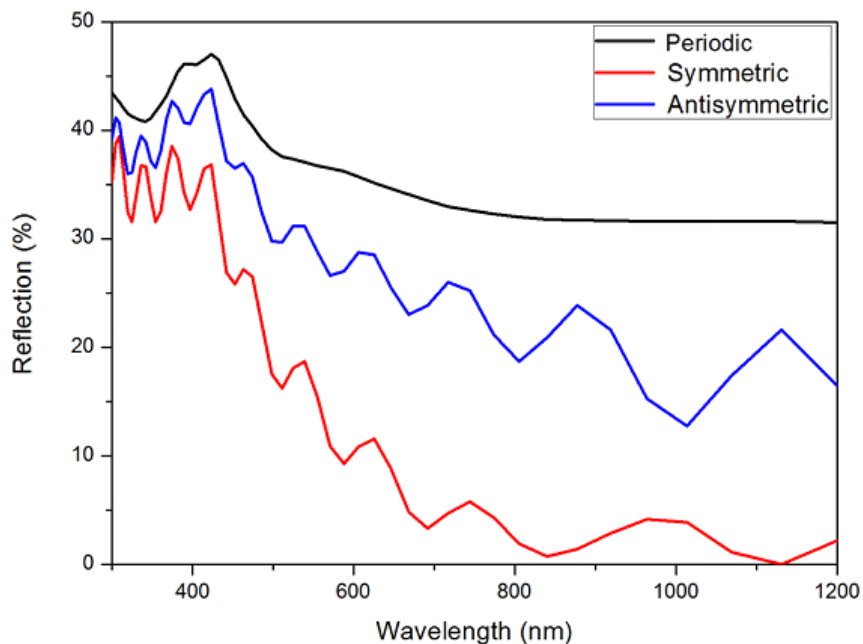


Fig. 5. Comparison the symmetric, antisymmetric and periodic BCs

3. CONCLUSIONS

Appropriate choice of boundary conditions is necessary to obtain correct results for the modeling of the photonic structures. Contemporary tools for numerical analysis offer several different boundary conditions. It is the responsibility of the user, to select the right BCs, based on the structure geometry and properties.

Acknowledgement

Calculations have been carried out in Wrocław Centre for Networking and Supercomputing (<http://www.wcss.pl>), grant No. 67

This research was supported with the Statutory Grant of the Faculty of Microsystem Electronics and Photonics, Wrocław University of Science and Technology.

References

- [1] Boundary condition. (n.d.) American Heritage® Dictionary of the English Language, Fifth Edition. (2011). Retrieved October 12 2017 from <https://www.thefreedictionary.com/boundary+condition>
- [2] Lumerical Solutions, Inc. <http://www.lumerical.com/tcad-products/fdtd/>, 19.09.2017
- [3] Using the boundary conditions tab, https://kb.lumerical.com/en/ref_sim_obj_boundary_conditions_tab.html, 19.09.2017
- [4] Yen-Yu Chou et al., Fabrication of sub-wavelength antireflective structure to enhance the efficiency of InGaAs solar cells, AUSMT, Published online 1 December 2014.
- [5] Przybylski D., Patela S., Numerical analysis of influence two-dimensional photonic crystal for efficiency of solar cell, 4th International Conference on Advances in Electronic and Photonic Technologies: proceedings of ADEPT, Tatranská Lomnica, Slovakia, 2016, p. 232-235.

THE FLOW SYSTEM FOR THE NON-ENZYMATIC DETERMINATION OF UREA

Sz. Sobota*, K. Malecha

Faculty of Microsystem Electronics and Photonics, Wrocław University of Science and Technology,
Janiszewskiego 11/17, 50-372 Wrocław, Poland
*e-mail: 212481@student.pwr.edu.pl

Abstract: *The article presents a microfluidic system used to determine the concentration of urea in biological substances. Modern methods of medical diagnostics should be uncomplicated, fast and cheap. The answer to these requirements in the case of urea analysis is the flow system for the non-enzymatic determination of urea. The article introduces its design and fabrication method using min. LTCC and 3D printing technology. The system was tested and the results presented and discussed in the article.*

Keywords: LTCC, Lab-on-chip, μ TAS, microfluidic system, urea determination

1. INTRODUCTION

Methods used in today laboratories consist of a number of different activities: taking a sample, conducting a suitable biological or chemical reaction, isolating and labeling products. Typically, each step of the process is carried out in a separate machine, that requires a sufficiently large laboratory. The answer to these and other problems became the usage of Micro Total Analyzing Systems (μ TAS), namely miniature analytical systems (or analytical microsystems) or Lab-on-chip systems. Their task is to perform various analyzes and biological or chemical reactions. Such systems have many advantages that standard laboratories do not have. First of all, these systems are miniaturized, which often helps to reduce the size of the lab to the size of a small box. They work on samples of micro- or nanoliter volumes. This allows a significant reduction in the consumption of the reagents needed, and consequently also the waste. The smaller the scale of the process, the less time it needs to determine certain substances. In short, this technology is cheaper, faster and safer. One of the biochemical tests performed in laboratories is the determination and measurement of urea concentration in biological substances such as blood and urine. This measurement is important for many medical diagnoses, so improving the process, reducing its cost and complexity, and accelerating the test, will make it much more effective in detecting many conditions and optimizing the course of treatment. The solution is to build a microsystem for the determination of urea.

2. METHODS AND MATERIALS

The purpose of the system is to calculate the concentration of urea in the biological substance by the method of absorbance. To achieve that, the test substance and the demethylglyoxime are delivered to the system with which the urea reaction produces a yellow product having the property of absorbing light. According to Jung's experiment, the best results are obtained using light at 480-540 nm wavelength [1].

2.1 Microfluidic module

The heart of the system is the miniature microfluidic module made using LTCC (Low Temperature Co-firing Ceramic) technology. It was chosen for its biological properties and chemical resistance, price and ease of integration of electronic and optoelectronic components. "LTCC technology enables the implementation of microfluidic systems with properties that are close to the most commonly used silicon systems" [2]. The created module and its X-ray image are showing the inside of the module in Figure 1.

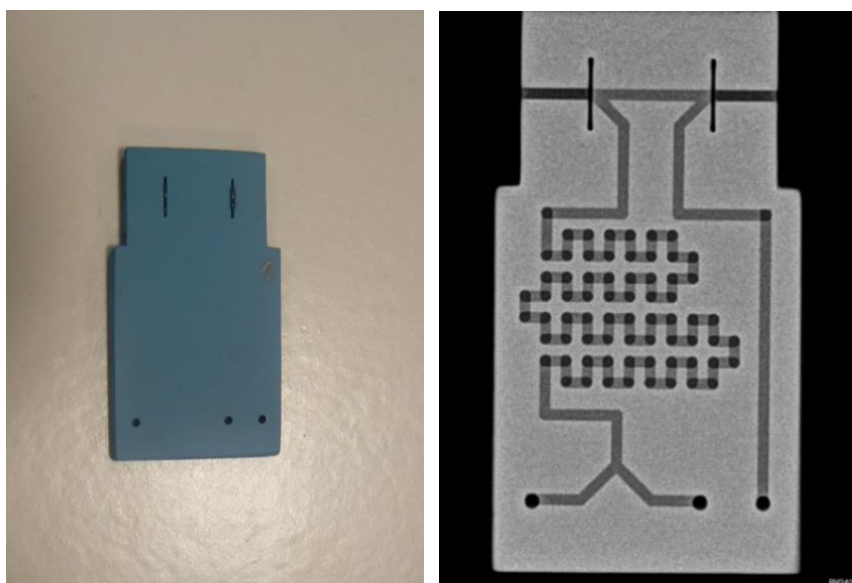


Fig.1. Microfluidic module and its X-ray photo

Channels with a width of $750\ \mu\text{m}$ have been designed. In the central part of the a micromixer module with a step structure is planned, in which the mixing of the constituent substances and their reaction with each other. Due to the low Reynolds number in micro and nano liquids, it is necessary for its correct occurrence. Behind it is a measuring channel. At its sides, two recesses were implemented in which glass plates of soda glass were placed. Their task is to seal the module while ensuring the propagation of light radiation.

2.2 Other components of the system

The microfluidic module was placed in a specially designed, polymer casing, made in the spatial printing technique. The lower and upper part of casing are shown in Figure 2.

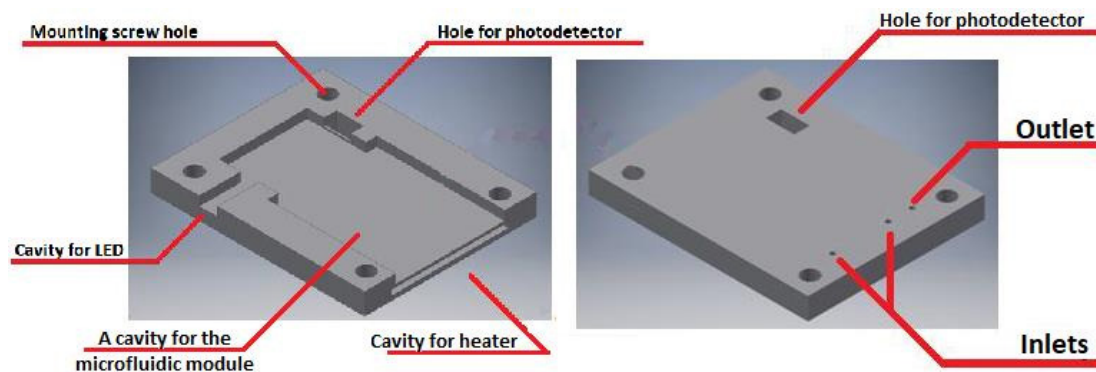


Fig. 2. The lower and upper part of polymer casing

The entire module was sealed with a PDMS (Polydimethylsiloxane) sealing gasket and then a liquid conduit system with inlets was mounted. Since the target chemical reaction needed to effectively detect urea must be carried out at about 80 ° C, instead of using an external temperature control method, it was decided to add a heater. It was made on a ceramic substrate, on which a conductive paste (PdAg) was applied by screen printing and formed into a resistive path. In addition, an optoelectronic elements: light emitting diode with wavelength 480 nm and photodetector was mounted. The complex whole is shown in Figure 2.

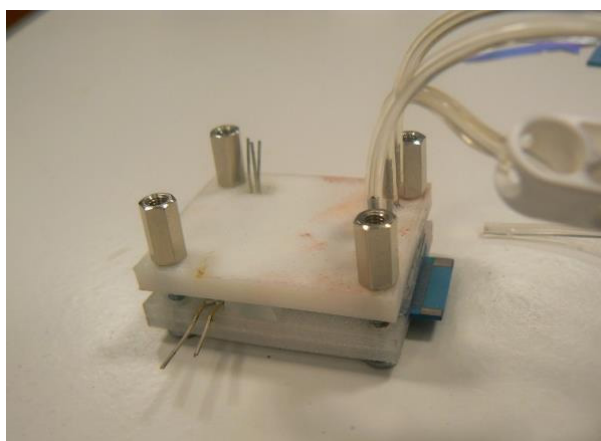


Fig. 3. The flow system for the non-enzymatic determination of urea

2.3 Measurement procedure

Determination of urea concentration in the substance takes place by measurement of absorbance. Using the Lambert-Beer law, we can calculate the concentration of the test solution based on it. Absorbance is a measure of the absorption of radiation, so it is the ratio of the input radiation intensity I_0 to the intensity of the output radiation I and is given by formula (1).

$$A = \log\left(\frac{I_0}{I}\right) \quad (1)$$

The law also shows that the absorbance is directly proportional to the concentration of the solution c and the optical path l through which the light passes, as recorded by the equation (2).

$$A = k * l * c \quad (2)$$

Where k is the absorption coefficient. Thus, knowing the intensity of the input and output radiation, the concentration of the test solution can be calculated [3].

A series of measurements was made. For this purpose, two sets of test solutions were prepared in which they were used dyes with light absorption similar to the reaction product: cochineal red (best absorption at wavelength 490 nm) and yellow orange (best absorption at 475 nm). They were mixed in several different concentrations with distilled water to obtain solutions of different colors, in assumptions showing different absorption of light radiation. Dyes mixed with 20,000mg distilled water in the following amounts:

- 0 mg (0%) – pure distilled water
- 1 mg (0.005%)
- 2 mg (0.01%)
- 4 mg (0.02%)
- 7 mg (0.035%)
- 14 mg(0.07%)
- 98 mg(0.5%)

The measuring station and its diagram are shown in Figure 4.

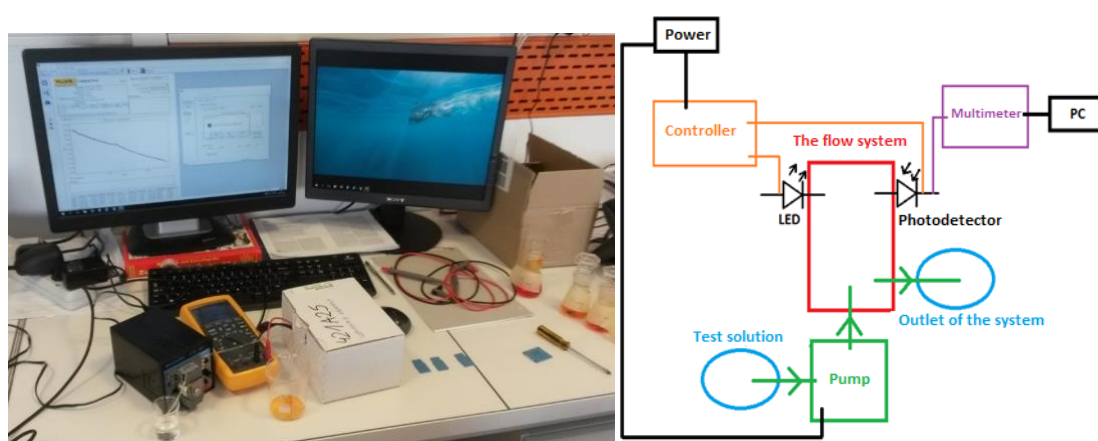
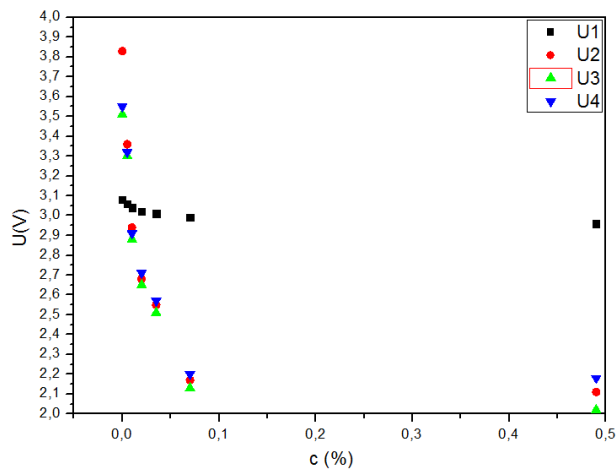


Fig.4. Measuring station and its scheme

2.4 Results

Four different microfluidic modules were tested. The photodetector response to different concentrations of solutions flowing through the module was measured. The result of the measurement is presented in Figure 5. Then the repeatability of the system response was checked, by passing alternately through the system clean distilled water and the solution with the maximum concentration. The result of the measurement is shown in Figure 6. Based on the Lambert-Beer law, the absorbance of solutions was calculated in dependence on the concentration of the solution. The graph is shown in Figure 7.



7.

Fig. 5. Measurement of the photodetector's response to different concentrations of solution flowing through the system

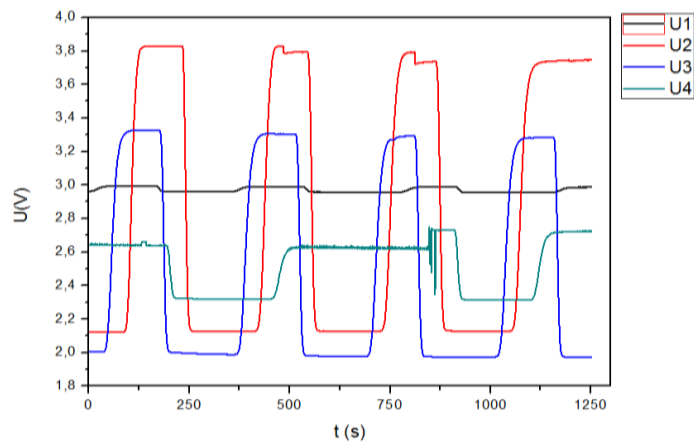


Fig. 6. Repeatability of response as photodetector voltage variation over time

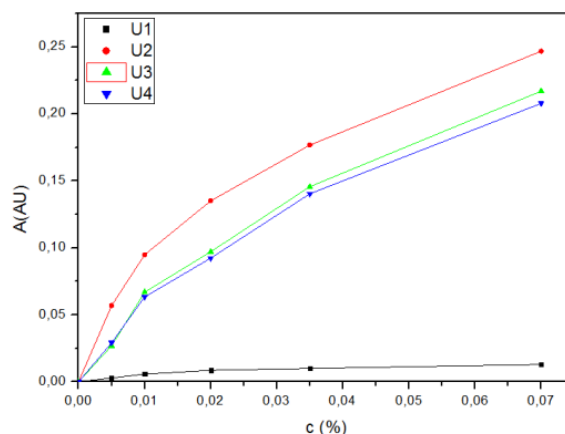


Fig. 7. Graph of the absorbance calculated from the Lambert-Beer law as a function of the solution concentration

The results derived from the carried out measurements show that the three of the executed microfluidic modules behave correctly. The exception to this is the Number 1 system, with black color on the charts, which reacts on changes of the concentration of the solution by very slight changes in the photodetector. Probably the reason is the insufficient amount of light passing through the circuit. Other systems behave comparably and repeatedly. The most important graph is the last one, as shown in Figure 6. It shows that the system fulfills the task entrusted to it and allows determination of urea concentration by measuring absorbance.

3. CONCLUSIONS

The purpose of the system was to determine in predictable and reproducible manner the concentration of the substance in the solution by the absorbance measurement method. The device is working properly and meets these requirements and can be successfully labeled Lab-on-chip or μ TAS. However, the presented system is only a prototype, so many of its components could be improved, such as improving the response rate of the system or reducing the impact of external factors such as light on measurements. However, the existing system is fully ready for real tests involving biological substances such as blood or urine.

References

- [1] D. Jung, H. Biggs, J. Erikson, P. U. Ledyard, „*New Colorimetric Reaction for End-Point, Continuous-Flow, and Kinetic Measurement of Urea*”, Indianapolis, 1975 r.
- [2] K. Malecha, „*Systemy mikroprzepływowe wykonane techniką LTCC*”, Wrocław, 2009 r.
- [3] E. Remiszewska, K. Malecha, J. Kruk, W. Torbicz, D. Pijanowska, „*Colorimetric method of urea determination with use of LTCC based microfluidic system*”, Wrocław, 2016 r.

AUTHOR INDEX

Antończak, A. J.	14	Nyk, M.	47
Ćwikła, M.	7	Owczarzak, S.	66
Dzienny, P.	14	Paszkiewicz, B.	21
Fiedot-Toboła, M.	41, 53	Paszkiewicz, R.	26, 66, 71
Glinkowski, M.	21	Patela, S.	80
Golonka, L.	31	Piejko, A.	71
Ilgiewicz, G.	26	Podwin, A.	76
Indyka, I.	31	Prażmowska, J.	71
Jasiński, M.	37	Przybylski, D.	80
Knapkiewicz, P.	59	Rac-Rumijowska, O.	41
Kuc, E.	41	Reiner, J.	7
Macherzyński, W.	26	Sąsiadek, E.	41
Macioszczyk, J.	31	Sobota, Sz.	86
Malecha, K.	53, 86	Stafiniak, A.	66
Nawrot, K. C.	47	Teterycz, H.	41
Nawrot, W.	53	Zakrzewski, A.	7
Niemczuk, J.	59		